Computational and experimental studies of reactive intermediates in glycosylation reactions

Remmerswaal, W.A.

Chapter 2 |

Origin of Stereoselectivity in S_E2' Reactions of Six-membered Ring Oxocarbenium Ions

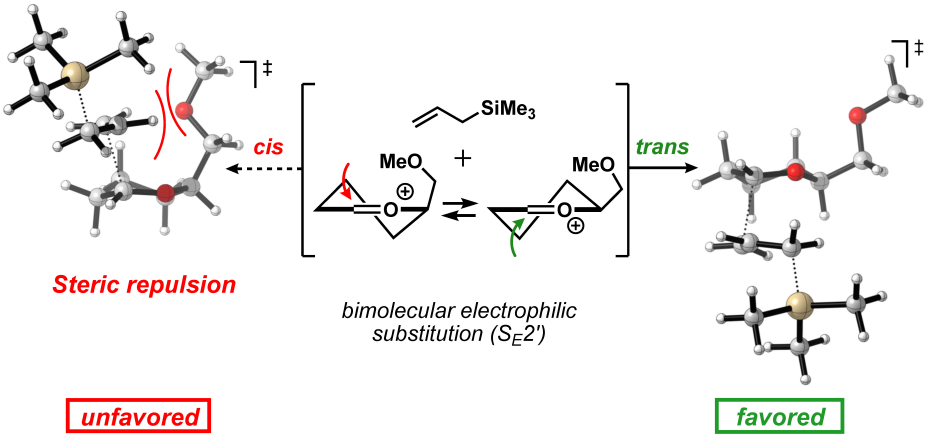

Abstract | Oxocarbenium ions are key reactive intermediates in organic chemistry. To generate a series of structure–reactivity-stereoselectivity principles for these species, herein the bimolecular electrophilic substitution reactions (S_E2') between allyltrimethylsilane and a series of archetypal six-membered ring oxocarbenium ions was investigated using a combined density functional theory (DFT) and coupled-cluster theory approach. These reactions preferentially proceed following a reaction path where the oxocarbenium ion transforms from a half chair ($^3H_4$ or $^4H_3$) to a chair conformation. The introduction of alkoxy substituents on six-membered ring oxocarbenium ions dramatically influences the conformational preference of the canonical $^3H_4$ and $^4H_3$ conformers, which influences the stereochemical outcome of the S_E2' reaction. In general, the stereoselectivity in the reactions correlates to the "intrinsic preference" of the cations, as dictated by their shape. However, for the C5-CH_2OMe substituent, steric factors override the "intrinsic preference" showing a more selective reaction than expected based on the shape of the ion. The S_E2' energetics correlate well with experimentally observed stereoselectivity, and the use of the activation strain model has enabled us to quantify important interactions and structural features that occur in the transition state of the reactions to precisely understand the relative energy barriers of the diastereotopic addition reactions. The fundamental mechanistic insight provided in this study will aid in understanding the reactivity of more complex glycosyl cations featuring multiple substituents and will facilitate the general understanding of glycosylation reactions.

Published | Remmerswaal, W. A.; Hansen, T.; Hamlin, T. A.; Codée, J. D. C. *Chem. Eur. J.* **2023**, *29* (14), e202203490.

Introduction

Six-membered ring oxocarbenium ions are important reactive intermediates in bioorganic and synthetic organic chemistry.[1–7] Carbohydrate processing enzymes, such as glycosyltransferases and hydrolases, transfer or cleave carbohydrates to or from their substrates. These reactions proceed through transition states, in which a significant amount of oxocarbenium character builds up in the carbohydrate moiety that is transferred or cleaved.[8,9] In synthetic carbohydrate chemistry, the stability of oxocarbenium ions determines the reactivity of glycoside donor building blocks and plays a central role in the stereochemical outcome of glycosylation reaction.[10–17] Despite the high reactivity of these species, they can react with excellent stereoselectivity, and it has been shown that many glycosyl oxocarbenium ions can provide reaction products with striking 1,2-*cis* selectivity.[18–22] The fleeting nature of oxocarbenium ions represents a major challenge in studying these species and determining clear structure-reactivity-stereoselectivity principles. Recently, direct spectroscopic evidence for glycosyl oxocarbenium ions has been provided in the gas phase using state-of-the-art IR spectroscopy and in super acid media (to guarantee a sufficient lifetime of the species) using NMR spectroscopy.[23–32] DFT calculations have provided detailed insight into the stereoelectronic effects of the substituents on the structure, stability and reactivity of these ions.[33–37]

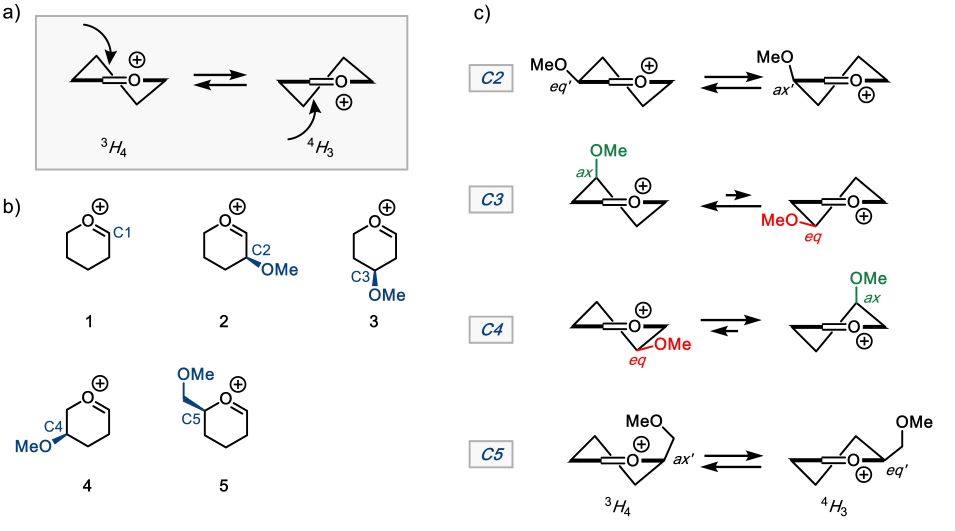

Scheme 1. (a) The conformational equilibrium between the $^3H_4$ and $^4H_3$ with the face preference following a chair-like TS; (b) Computationally analyzed substituted oxocarbenium ions, *i.e.*, cation **1**-**5**; (c) Conformational preference (green = stabilizing; red = destabilizing) of mono-substituted six-membered oxocarbenium ions reflected by the isolated product ratios (*i.e.*, diastereoselectivity) from the seminal work of Woerpel *et al.*,[38,39] in which ax(') = (*pseudo*-)axial and eq(') = (*pseudo*-)equatorial.

Generally, oxocarbenium ions adopt a flattened structure, as a consequence of the stabilization of the electron-depleted cationic carbon by the adjacent electron-rich ring-oxygen, adopting a $^3H_4$ or $^4H_3$ conformation (Scheme 1a).[40] It has been proposed that these half chair conformers are preferentially attacked at the diastereotopic face that leads to a low energy chair-like transition state as opposed to the other face, which provides a twist boat-like transition state (Scheme 2).[41,42] Consequently, the $^3H_4$ will form a top-face product (Scheme 1a), while a bottom-face product is found for the opposite $^4H_3$ half chair. It is known

that substituents on the ring can dramatically affect the conformational preference of the six-membered cation, and thus the stereochemical outcome of reactions with these cations.[43–46] Substituted cyclic oxocarbenium ions with electron-rich substituents (*e.g.*, *O*-, *N*-, *F*-groups) at the C3- and C4-position of the ring prefer to adopt an axial position, presumably to stabilize the cationic center by electrostatic and orbital interactions (Scheme 1b and 1c).[38,39] When these groups are present on the C2-position, they have a very slight preference to adopt a *pseudo*-equatorial position, enabling hyperconjugative stabilization by the *pseudo*-axial σ_{C2-H2} bond of the oxocarbenium ion. Despite spectroscopic and computational studies that have provided a detailed understanding of the conformational behavior of six-membered oxocarbenium ions,[18–22] quantitative insight into the factors controlling the reactions taking place on these ions is largely lacking.

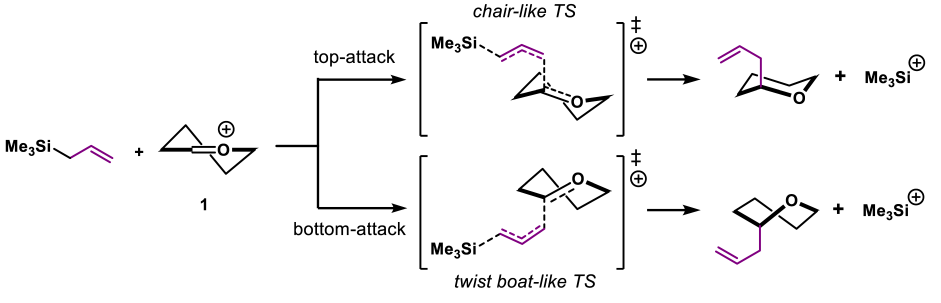

Scheme 2. Top face-attack (*i.e.*, chair-like TS) and bottom face-attack (*i.e.*, twist boat-like TS) of the S_E2' reaction between allyltrimethylsilane and $^3H_4$ oxocarbenium ion **1**. The reaction follows a transfer reaction by a bimolecular electrophilic substitution mechanism (S_E2'), in which an allylic-group (purple) is transferred between two electrophilic moieties.[47]

To study how stereoelectronic effects impact the stereoselectivity of the reactions involving six-membered oxocarbenium ions, the reaction profile of reactions between allyltrimethylsilane and a series of oxocarbenium ions **1-5** was explored using density functional theory at PCM(CH_2Cl_2)-B3LYP/6-311G(d,p) (Scheme 1b and Scheme 2). Additionally, high accuracy DLPNO-CCSD(T)[48] reference data were computed, confirming the reliability of the DFT method. Allyltrimethylsilane was selected as a typical *C*-nucleophile that requires a strong electrophile, such as an oxocarbenium ion intermediate, to react.[18–22] These reactions follow a bimolecular electrophilic substitution reaction path (S_E2'), in which an allylic-group (purple in Scheme 2) is transferred to the electrophilic oxocarbenium ion by the expulsion of the electrophilic Me_3Si^+ leaving-group.[49–52] The analyzed oxocarbenium ions **2-5** have a single ring substituent on the six-membered ring at the C2-, C3-, C4-, or C5-position (see Scheme 1b), to map the effects of these substituents as a function of their position in the ring. To furnish quantitative insight into the electronic factors governing in these S_E2' reactions, the activation strain model (ASM)[53,54] and Kohn-Sham molecular orbitals (KS–MO) was employed.[55–57]

Results and Discussion

Structure and Reactivity Trends

The results of the computed reaction profiles and structural data of the S_E2' reaction between allyltrimethylsilane and cations **1-5** are summarized in Figure 1 – 3 (for interested readers, all the data on the stationary points can be found in Table S1, S2 and S3). Note that all reactivity trends are consistent for ΔG and ΔE (Table S1). Importantly, the computed trends in reactivity at PCM(CH_2Cl_2)-B3LYP/6-311G(d,p) agree well with computed energies at the more accurate SMD(CH_2Cl_2)-(TightPNO)DLPNO-CCSD(T)/CBS(3,4/def2) level (Table S1 and S2).[58] Figure 1 shows the structures of the two possible transition states following a chair-like or twist boat-like TS of cation **1**, in which both electrophilic species, *i.e.*, trimethylsilyl leaving group and oxocarbenium ion, are orientated in an antiperiplanar fashion, both interacting with the allyl moiety (highlighted in purple in Figure 1). As anticipated, for cation **1** that the chair-like TS is more than 4 kcal mol^{-1} lower in energy than the reaction barrier of the twist boat-like TS using DFT computations (Table S1 and S2 for all reaction profile data).

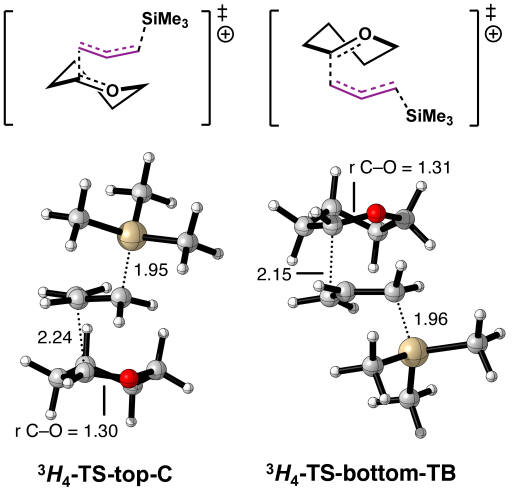

Figure 1. Transition state structures with key bond lengths (in Å) for the S_E2' reactions between allyltrimethylsilane and oxocarbenium ion **1** following a top face-attack, *i.e.*, chair-like TS, and bottom face-attack, *i.e.*, twist boat-like TS, computed at PCM(CH_2Cl_2)-B3LYP/6-311G(d,p).

For the unsubstituted oxocarbenium ion **1**, the $^3H_4$ and $^4H_3$ structures are chemically equivalent, but introducing a substituent on the six-membered ring gives rise to two chemically different structures. It was found that these two reactants, $^3H_4$-R and $^4H_3$-R, are in rapid equilibrium with each other by a relatively low interconversion barrier via the $B_{2,5}$ or $^{2,5}B$ conformer, setting the stage for a Curtin-Hammett scenario (Figure 2 and 3).[59,60] In this case, the reaction barrier difference, $\Delta\Delta G^{\ddagger}$, dictates the product distribution. If (i) $\Delta G^{o}{}_{^3H_4}$ is lower in energy than $\Delta G^{o}{}_{^4H_3}$, as for cation **2** and **3**, $\Delta\Delta G^{\ddagger} = (\Delta G^{\ddagger}{}_{^4H_3\text{-bottom}} + \Delta G^{o}{}_{^4H_3}) - \Delta G^{\ddagger}{}_{^3H_4\text{-top}}$, while if (ii) $\Delta G^{o}{}_{^3H_4}$ is higher in energy than $\Delta G^{o}{}_{^4H_3}$, as for cation **4** and **5**, $\Delta\Delta G^{\ddagger} = \Delta G^{\ddagger}{}_{^4H_3\text{-bottom}} - (\Delta G^{\ddagger}{}_{^3H_4\text{-top}} + \Delta G^{o}{}_{^3H_4})$.[61]

Several distinct trends emerge from the computed reaction profiles for cations **2-5** **(**Figure 2 and 3). Firstly, in line with cation **1**, cation **2-5** all favor the chair-like TS over the twist boat-like TS ($\Delta\Delta G^{\ddagger}_{\text{twist boat-chair}}$ = ~ +3–5 kcal mol^{-1}). This reinforces the notion that the half chair conformers exclusively react via the chair-like TS for these model systems. Secondly, the lowest overall reaction barrier found for the different cations decreases from +12.4, +12.1, +10.9, +8.4 kcal mol^{-1} for mono-substituted cations **5**, **4**, **3**, **2** (substituent at the C5, C4, C3, or C2 position respectively, Figure 1b), placing the alkoxy substituent gradually closer in space to the electrophilic C1-position (respectively 4.10, 3.32, 3.11, and 2.37 Å in the equilibrium geometry). The lower reaction barrier is a direct effect of the electron-withdrawing character of the substituent, which gradually increases the electron-accepting capability of the C1-cation along the cation series. For all systems, there is a parallel between the $\Delta\Delta G^{\ddagger}$ of the overall reactions and the lowest energy oxocarbenium ion conformer (highlighted in purple in Figure 2 and 3). These findings are in line with previous work, in which the stereoselectivity in addition reactions of allyltrimethylsilane and triethylsilane could be related to the conformational preference of pyranosyl and furanosyl oxocarbenium ions.[18–22] Cation **3** (3-OMe) favors the $^{3}H_4$ conformation, which is attacked from the top face, resulting in a *cis*-product (Figure 3b). In contrast, cations **4** and **5** prefer the opposite $^{4}H_3$ half chair, which preferentially reacts on the bottom face (Figure 2d and 3b), delivering the *trans*-product. Note, that cation **5** only has a very slight preference for the $^{4}H_3$. Cation **2** has no clear preference for either half chairs, which results in a mixture of *cis*- and *trans*-products (Figure 3d). Overall, the computed stereoselectivity, derived from the $\Delta\Delta G^{\ddagger}$ values, correlates well with the available experimental result by Woerpel and co-workers.[38,39]

Importantly, differences are observed between the conformational preference of the cation ($\Delta\Delta G^{o}$) and the relative differences of the overall barriers ($\Delta\Delta G^{\ddagger}$), which will be explained in detail. For example, Figure 3b shows that cation **5** has a very small preference for the $^{4}H_3$ conformation over the $^{3}H_4$ ($\Delta\Delta G^{o}$ = –0.4 kcal mol^{-1} for the $^{4}H_3$ relative to the $^{3}H_4$), but the relative overall reaction barriers for the two $^{1}C_4$ and $^{4}C_1$ chair like-like TSs, originating from respectively the $^{3}H_4$ or the $^{4}H_3$ conformer, show a larger difference ($\Delta\Delta G^{\ddagger}$ = –2.1 kcal mol^{-1}). This difference leads to a more *trans*-selective reaction than what would be expected based on the intrinsic conformational preference of the cation.

The difference in energy of the two conformers of cation **4** (Figure 2d, $\Delta\Delta G^{o}$ = –2.0 kcal mol^{-1} for the $^{4}H_3$ relative to the $^{3}H_4$) is partly diminished in the transition states of the S_E2' reactions originating from these ($\Delta\Delta G^{\ddagger}$ = –1.0 kcal mol^{-1}). For cation **3** (Figure 2b), it was found that the difference in the reaction barriers ($\Delta\Delta G^{\ddagger}$ = +2.0 kcal mol^{-1} for the $^{4}H_3$ relative to the $^{3}H_4$) is significantly larger than the conformational preference of the cation ($\Delta\Delta G^{o}$ = +1.1 kcal mol^{-1}). For cation **2** (Figure 3d), there is no clear preference between both half chair conformers ($\Delta\Delta G^{o}$ = +0.1 kcal mol^{-1} for the $^{4}H_3$ relative to the $^{3}H_4$), and also the corresponding transition states show only a marginal difference ($\Delta\Delta G^{\ddagger}$ = –0.2 kcal mol^{-1} for the $^{4}H_3$ relative to the $^{3}H_4$).

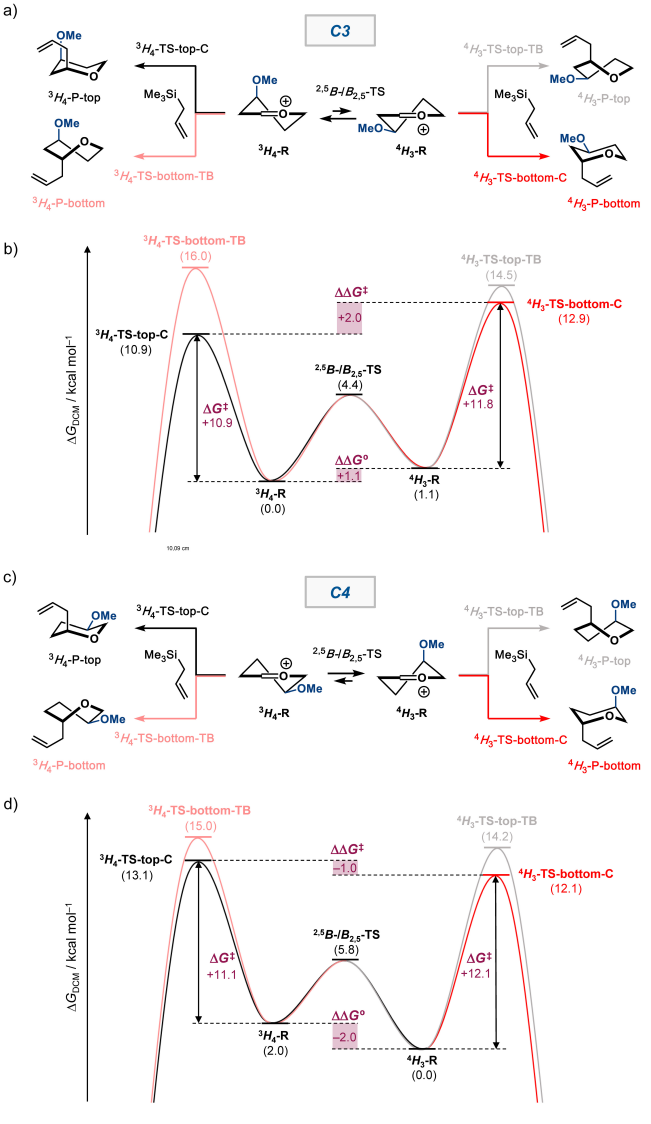

Figure 2. The possible S_E2' reaction pathways and the corresponding reaction profile of cation **3** (a,b) and **4** (c,d) of the top- (black: chair-like TS path, grey; twist boat-like TS path) and bottom attack (red: chair-like TS path; pink: twist boat-like TS path) at the $^3H_4$ and $^4H_3$ conformations. Gibbs energies in dichloromethane (ΔG_{DCM}, in kcal mol^{-1}) relative to reactants. See SI Table S1 for all data of the stationary points of the reaction profiles, including the products.

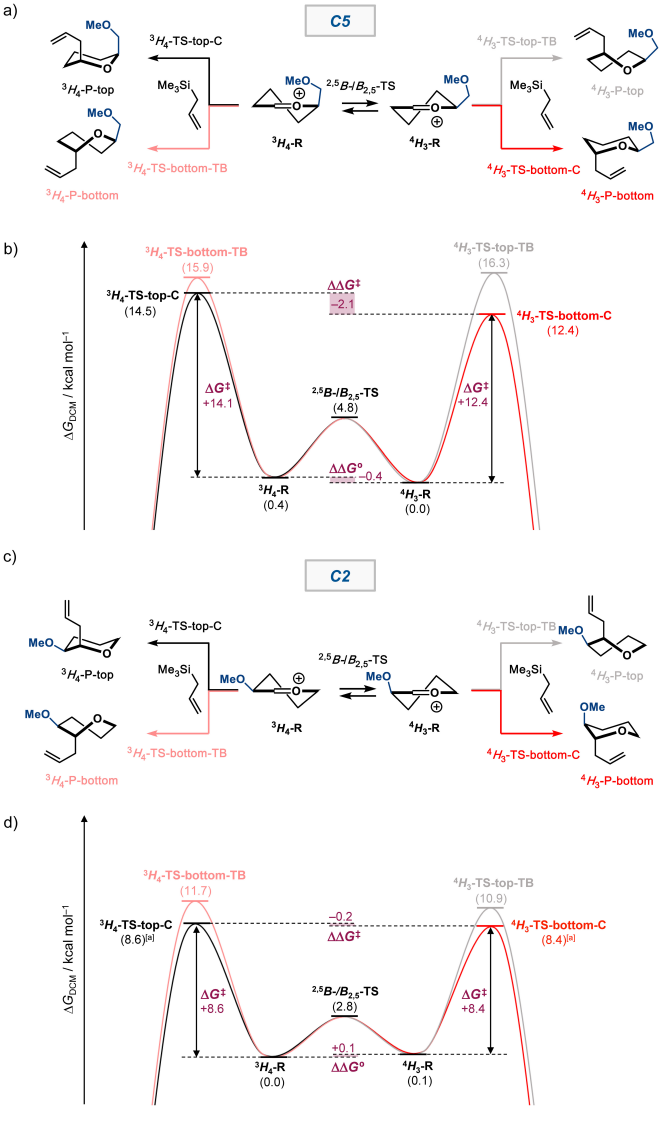

Figure 3. The possible S_E2' reaction pathways and the corresponding reaction profile of cation **5** (a,b) and **2** (c,d) of the (black: chair-like TS path; grey: twist boat-like TS path) and bottom attack (red: chair-like TS path; pink: twist boat-like TS path) at the $^3H_4$ and $^4H_3$ conformations. Gibbs energies in dichloromethane (ΔG_{DCM}, in kcal mol^{-1}) relative to reactants. See SI Table S1 for all data of the stationary points of the reaction profiles, including the products. [a] Reaction barriers could not be located on the electronic energy surface, and an accurate approximation of the barrier was made based on the Gibbs energy surface (see methods section in the SI for details).

Activation strain analyses

To gain quantitative insight into the physical factors controlling the facial selectivity of the additions to either face of the half chair conformations (*i.e.*, the chair-like TS versus the twist boat-like TS), the activation strain model (ASM) of reactivity was employed.[55,56,62] The ASM is a fragment-based approach in which the reaction profile can be described with respect to, and understood in terms of, the characteristics of the reactants, *i.e.*, allyltrimethylsilane and the oxocarbenium ion (see method section for more details). The ASM decomposes the total energy (ΔE) into strain energy (ΔE_{strain}) and interaction energy (ΔE_{int}). The strain energy can be understood as the energy penalty incurred due to deformation of the individual fragments, while the (generally net-stabilizing) interaction energy can be understood as the interactions (destabilizing Pauli repulsion and stabilizing electrostatic and orbital interactions) between the fragments. In the herein presented activation strain diagrams (ASDs), the intrinsic reaction coordinate (IRC) is projected onto the carbon–leaving group (C•••Si) stretch. This critical reaction coordinate undergoes a well-defined change during the reaction from the reactants via the transition state to the product and is shown to be a valid reaction coordinate for studying bimolecular reactions.

Figure 4a shows that the top face-attack (black line) at the unsubstituted oxocarbenium ion **1** via a chair-like TS proceeds with a significantly lower barrier than the bottom face-attack (pink line) via a twist boat-like TS (see Figure S1, S2, and S3 for ASM data of the full reaction profile for all studied systems, both in solution and gas-phase). Figure 4 reveals that this facial selectivity originates from a more stabilizing interaction energy, which develops in the reaction pathway via the chair-like TS, while the strain curves are very similar for both faces of attack. The more stabilizing interaction energy is a direct effect of the more efficient deformation of the half chair to chair-like TS, as it does not lead to eclipsing interactions (Pitzer strain) between the C1–H and the *pseudo*-equatorial C2–H, in contrast to the twist boat-like TS (Figure 4b). The more efficient deformation allows the chair-like TS to have a larger degree of the pyramidalization of the C1-position, *i.e.*, C2–(H)C1=O$^+$, than the twist boat-like TS at the same C•••Si bond stretch. The pyramidalization is essential for the reaction progression as the C1-atom transforms from a trigonal planar (sp^2) geometry in the starting oxocarbenium ion into a tetrahedral (sp^3) geometry in the product.

The effect of this higher degree of pyramidalization on the reaction path preference can be well understood with the recently introduced concept of a reaction's "transition state acidity,"[62–67] which states that a more acidic substrate, possessing a LUMO of lower energy, will interact more strongly with a Lewis base (*i.e.*, electron-rich species). The LUMO of the oxocarbenium has mainly antibonding character in the C1=O$^+$ bond (red wiggle in Figure 4d). The elongation of the C–O bond along the reaction coordinate reduces this antibonding overlap, which leads to a stabilization of the LUMO orbital energy. The chair-like TS has a higher degree of pyramidalization than the twist boat-like TS, which results in a longer C1=O$^+$ bond of the oxocarbenium ion (C–O bond length: 1.311 Å and 1.306 Å for the chair-like and twist boat-like TS, respectively, at 0.049 Å C•••Si stretch). This increased C1=O$^+$ bond length reduces the antibonding overlap between p_z atomic orbitals of the C- and O-atom of the oxocarbenium ion, leading to a lower energy LUMO (more stabilized LUMO, Figure 4d). The resulting smaller $\text{HOMO}_{\text{allyltrimethylsilane}}$–$\text{LUMO}_{\text{cation}}$-**1** translates to a more stabilizing orbital interaction (Figure 4c; see Figure S4 and Table S7 for EDA data).

One could expect that the more efficient deformation of the half chair to chair-like TS would also lead to less destabilizing strain for this reaction pathway. However, the more advanced pyramidalization for the chair-like TS at the same point on the reaction profile (at the same C•••Si bond stretch) as for the skew boat-like TS leads to an overall comparable strain development for both reaction pathways (Figure 4a).

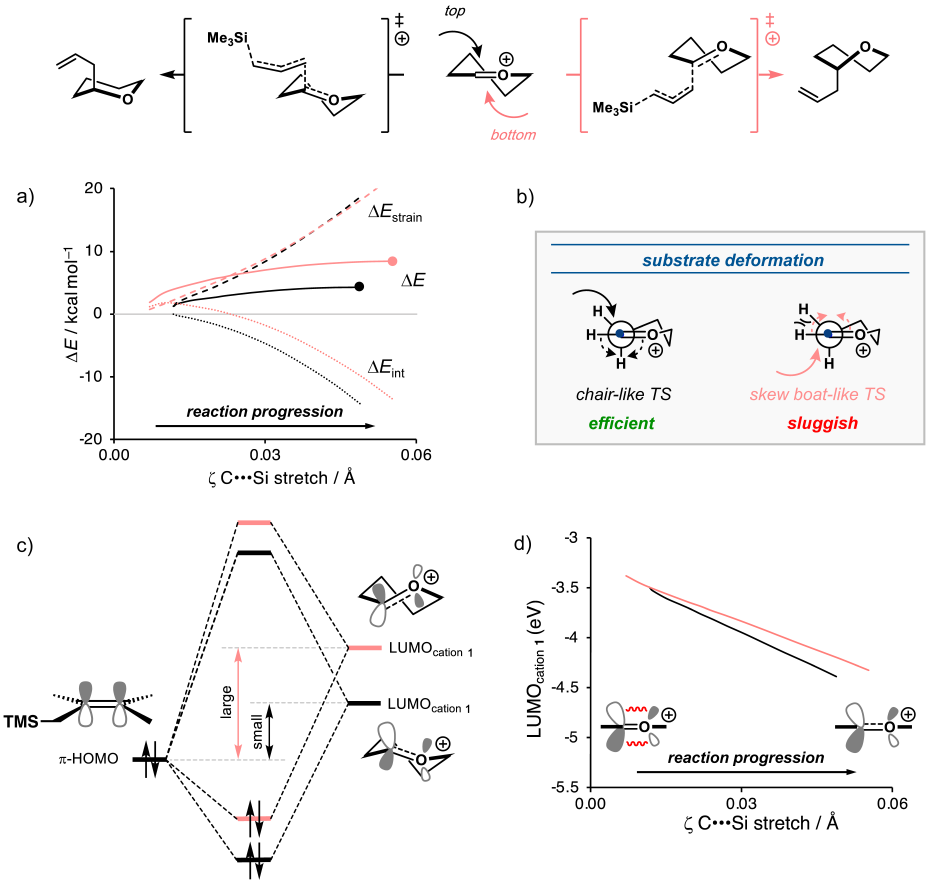

Figure 4. (a) Activation strain model and of the substrate for the S_E2' reactions of allyltrimethylsilane and cation **1** via the top face-attack (black: chair-like TS) and bottom face-attack (pink: twist boat-like TS), where the energy values are plotted to the transition state (indicated by a dot), along the IRC projected on the C•••Si bond stretch. (b) Schematic summary of the controlling factor of the facial selectivity of the oxocarbenium ion half chair conformation. (c) MO diagram of the most important donor–acceptor interaction between the π–$HOMO_{allyltrimethylsilane}$ and the $LUMO_{cation\ 1}$. (d) The LUMO energy ε (in eV) of the system described in the caption (a). Computed at COSMO(CH_2Cl_2)-ZORA-B3LYP/TZ2P//PCM(CH_2Cl_2)-B3LYP/6-311G(d,p).

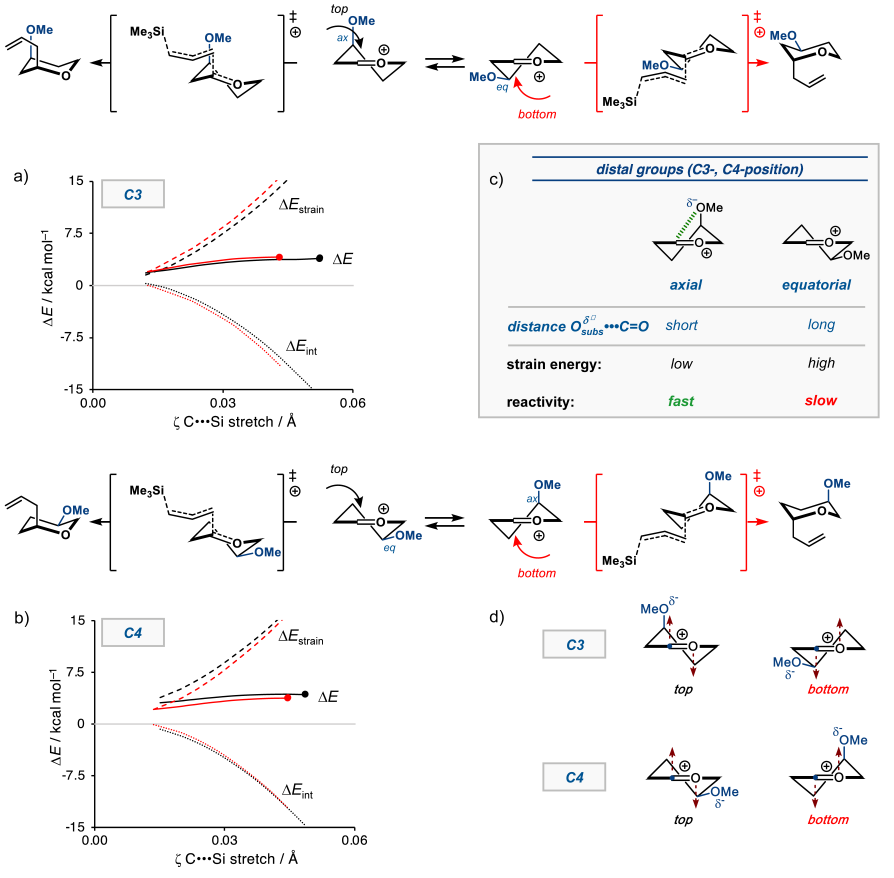

Figure 5. Activation strain model for the S_E2' reactions of allyltrimethylsilane + cation **3** (a) and **4** (b) via the top face-attack (black: chair-like TS) and bottom face-attack (red: chair-like TS), where the energy values are plotted to the transition state (indicated by a dot), along the IRC projected on the C•••Si bond stretch. (c) Schematic summary of the controlling factor of the stereoselectivity of the oxocarbenium ions with distal alkoxy substituents. (d) Movement of the C1=O$^+$ bond along the S_E2' reaction for cation **3** and **4**. Computed at COSMO(CH_2Cl_2)-ZORA-B3LYP/TZ2P//PCM(CH_2Cl_2)-B3LYP/6-311G(d,p).

After investigating the facial selectivity of the non-substituted half chair oxocarbenium ion, the factors that control the stereoselectivity of the substituted cyclic oxocarbenium ion **2-5** was analyzed by means of the ASM (see Table S7 for the ASM/EDA data on consistent geometries of **2-5**). Note, that in the following sections, the lowest energy conformer is used as reference energy in the activation strain diagrams (ASDs) for both reaction paths, because this is the most descriptive way to delineate the analysis of the trends in reactivity and allows a direct connection to the $\Delta\Delta G^{\ddagger}$ shown in Figure 2 and 3. Furthermore, focus will be solely on the pathways proceeding through a chair-like TS for both the $^3H_4$ (black line) and $^4H_3$ (red line) conformers, as the twist boat-like TSs are significantly higher in energy, and thus less relevant.

Figure 5a and 5b show the activation strain diagrams (ASDs) of the S_E2' reaction of allyltrimethylsilane with C3-OMe cation **3** and C4-OMe cation **4**, as these exhibit similar characteristics. For cation **3**, the top face-attack is the preferred pathway (black line), and the ASM analysis reveals that this preference originates from a less destabilizing strain energy for this pathway. For cation **4**, the bottom face-attack on the $^4H_3$-ion is favored (red line), which, likewise, can be traced back to the less destabilizing strain energy for this reaction path. For both cation **3** and **4** the developing interaction energy for the top and bottom face pathways is similar, and hence, does not account for the found reactivity trend.

By decomposing the total strain energy term into the strain energy of the individual reactants, it was found that the differences in strain energy solely originate from the oxocarbenium ion component and that the strain energy of allyltrimethylsilane is very similar for both reaction pathways (see Figure S6). The differences in strain of the oxocarbenium ions at the start of the reaction profile can be directly attributed to the conformational preference, *i.e.*, "intrinsic preference," of the oxocarbenium ion,[19] with the $^3H_4$ conformer being most stable for cation **3** and the $^4H_3$-conformer being the most stable for ion **4**.

Recall, that the lowest energy conformer as reference energy was used in the ASDs for both reaction paths. The addition to either face follows a similar reaction path through a chair-like transition state, providing strain curves with similar slopes, but the offset is significantly different as a result of the intrinsic stability of the conformation of the oxocarbenium ions (*i.e.*, "intrinsic preference"; Figure 5c).

Careful inspection of the strain curves reveals that the curves for cation **4** slightly converge along the reaction coordinate, while the curves for cation **3** slightly diverge. This difference in strain energy explains why the "intrinsic preference" of the cation ($\Delta\Delta G^\circ$) does not directly correlate to the difference in the corresponding overall reaction barriers ($\Delta\Delta G^\ddagger$) for these reactions. The divergence and convergence of the strain curves of the reactions can be traced back to the deformation of both half chairs along the reaction coordinate. For cation **3**, the top face-attack at the $^3H_4$ conformer brings the C1-atom closer to the stabilizing axial C3-OMe group (black path; Figure 5d), while this is not the case for the $^4H_3$ conformer (red path; see Figure S7 for more information), diverging the strain curves along the reaction coordinate. For cation **4**, the electrophilic anomeric C1-atom is pulled away from the stabilizing axial C4-OMe group in going from the $^4H_3$ conformer to the chair-like TS (red path), resulting in increased destabilization of the cation. This effect is significantly less for the reaction taking place with the $^3H_4$ conformer (black path), and as a result, the two strain curves converge along the reaction coordinate.

Next, attention was directed to the ASDs of the S_E2' reaction of allyltrimethylsilane with the oxocarbenium ions bearing the substituent closer to the C-1 atom, the C5-CH_2OMe cation **5** and the C2-OMe cation **2**. Oxocarbenium ion **5** preferentially undergoes a bottom face-attack, which, in line with the S_E2' reactions of cation **3** and **4**, can be traced back to the less destabilizing strain developing in this reaction pathway. However, the difference in strain energy between the top and bottom face reaction around the start of the reaction ($\Delta\Delta E$ $\sim$ –2 kcal mol^{-1} for the $^4H_3$ relative to the $^3H_4$ conformer) is significantly larger than the intrinsic energy difference between the $^3H_4$ and $^4H_3$ conformers ("intrinsic preference") of cation **5** (see Figure 3). By analyzing the reaction path for the top face-attack, which takes place on the $^3H_4$-cation, it becomes clear that allyltrimethylsilane comes in close proximity to the *pseudo*-axial C5-CH_2OMe-substituent, resulting in steric repulsion between the two reactants.

This steric repulsion can be minimized by bending the substituent away, leading to more destabilizing strain energy due to the deformation of the reactant along the complete reaction profile (see Figure S7c). Note that steric repulsion between the reactants can manifest in both: (i) the strain energy, because steric repulsion deforms the fragments, and (ii) the steric (Pauli) repulsion found in the nucleophile–electrophile interaction.[68] In this case the steric repulsion is primarily absorbed into the strain term, leading to additional deformation of the cation. The steric repulsion between the C5-CH_2OMe-substituent and allyltrimethylsilane renders cation **5** substantially more bottom face selective than what would be expected based on the intrinsic preference of the cation. Intuitively, one could expect a similar scenario for cation **3**, in which the axial C-3 substituent can also engage in steric interactions with the incoming allyltrimethylsilane. However, the C-3 OMe-substituent is significantly smaller than the C-5 CH_2OMe substituent, avoiding excessive steric repulsion.[69]

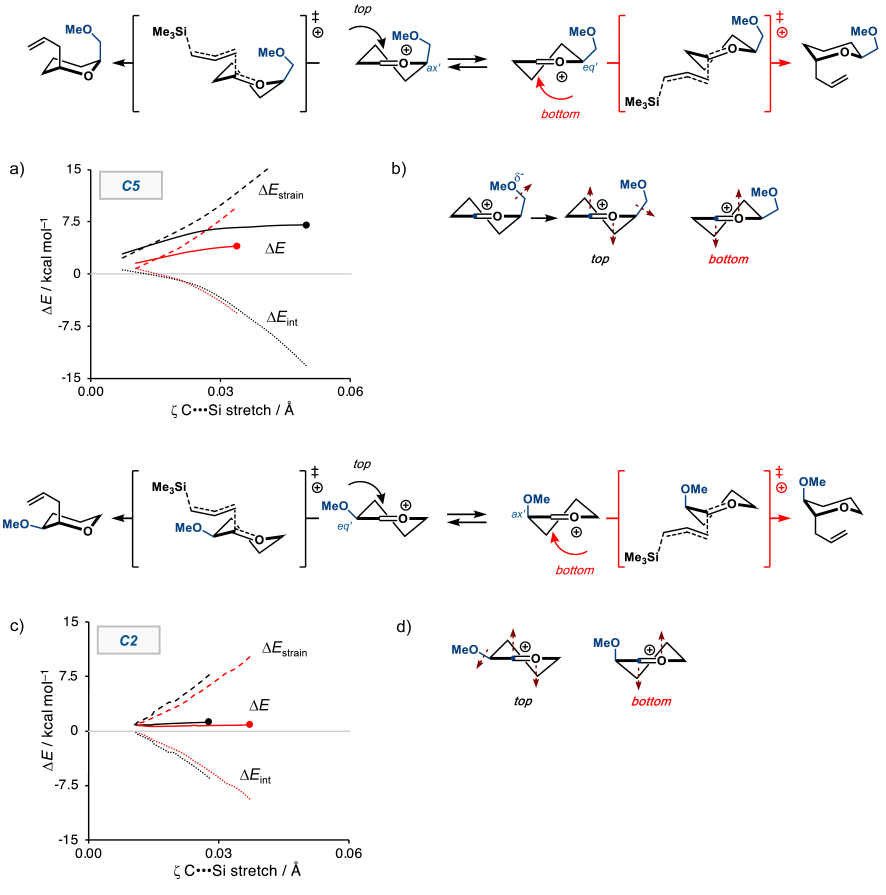

Figure 6. (a,c) Activation strain model for the S_E2' reactions of allyltrimethylsilane + cation **5** and **2** via the top face-attack (black: chair-like TS) and bottom face-attack (red: chair-like TS), where the energy values are plotted to either the transition state or a local maximum (indicated by a dot), along the IRC projected on the C•••Si bond stretch. (b,d) Movement of the C1=O$^+$ bond and substituent along the S_E2' reaction for cation **5** and **2**. Computed at COSMO(CH_2Cl_2)-ZORA-B3LYP/TZ2P//PCM(CH_2Cl_2)-B3LYP/6-311G(d,p).

Analogous to the strain curves for cation **4**, the strain curves for cation **5** slightly converge along the reaction coordinate. Again, this difference in strain energy stems from the deformation of both half chairs as the reaction progresses. For the transformation of the $^4H_3$ conformation to the chair-like TS (red path), the electrophilic anomeric C1-atom is pulled away from the stabilizing *pseudo*-axial C5-CH_2OMe group resulting in the overall destabilization of the cation (Figure 6b). This effect is less apparent for the reaction taking place on the $^3H_4$ conformer (black path).

Finally, the ASD of the reactions on the C2-OMe cation **2** shows that there is only a marginal difference in the transition state energies of the top- and bottom face reactions. The similar strain energy of the oxocarbenium ions at the start of the reaction profile is related to the similar energy of the $^3H_4$ and $^4H_3$-conformers (+0.1 kcal mol^{-1} for the $^4H_3$ relative to the $^3H_4$). The strain curves diverge upon the progression of the reaction coordinate, which can be explained by the 2-OMe bending away from the allylic moiety, which comes in from the same side, to minimize steric interactions. The bottom face approach avoids this steric interaction, resulting in a slightly lower reaction barrier for the bottom-face reaction (red pathway; $\Delta\Delta G^{\ddagger}$ = –0.2 kcal mol^{-1} for the $^4H_3$ relative to the $^3H_4$).

Conclusions

These computational investigation has revealed that S_E2' reactions of allyltrimethylsilane with six-membered oxocarbenium ions can follow reaction pathways proceeding with chair-like and twist boat-like transition states. For all studied cases, the chair-like TS has a significantly lower reaction barrier than the twist boat-like TS. The activation strain and Kohn-Sham molecular orbital theory analyses reveal that the facial preference for the chair-like TS, compared to the skew boat-like TS, originates from a more efficient geometric deformation (pyramidalization of C1) in transitioning from the half chair starting compound to the chair-like TS.

The introduction of alkoxy substituents on the six-membered oxocarbenium ion strongly impacts the stereochemical outcome and reactivity of the studied S_E2' reactions. Overall, the reaction barriers decreased by placing the alkoxy substituent systematically closer to the electrophilic C1-position. This lowering of the reaction barriers along the cation series is a direct effect of the electron-withdrawing effect of the substituent, which stepwise increases the electron-accepting capability of the C1-atom of the oxocarbenium ion. Moreover, the activation strain analyses showed that the stereoselectivity of the addition reactions of allyltrimethylsilane to the oxocarbenium ions is primarily set by the energy difference between the half chair conformers (*i.e.,* the "intrinsic preference" of the cations) as the most stable oxocarbenium ion conformers led to the lowest-energy reaction barrier. Strikingly, for the C5-CH_2OMe-substituted cation, it was found that steric interactions between the relatively large C5-substituent and allyltrimethylsilane developed, resulting in a significantly more *trans*-selective reaction for the C5-CH_2OMe cation, than what would be expected based on the relative energy of the two half chair oxocarbenium ions.

Overall, this study has dissected the effects at play during the addition of a typical *C*-nucleophile to mono-substituted six-membered oxocarbenium ions. The fundamental mechanistic insight provided in this contribution will be helpful in understanding the reactivity of more complex glycosyl cations featuring multiple substituents and will aid in the general understanding of glycosylation reactions.

Supporting information

Computational Methods

Using density functional theory (DFT), the potential energy surfaces (PES) of non-substituted oxocarbenium cation **1** and mono-substituted cation **2** (2-OMe), **3** (3-OMe), **4** (4-OMe), **5** (5-CH_2OMe) and **6** (6-OMe) were calculated. The DFT computations were performed using Gaussian 09 rev D.01.[70] For all computations, the hybrid functional B3LYP[71–73] and the 6-311G(d,p)[74] basis set were used. The geometry convergence criteria were set to tight (opt=tight; max. force=$1.5\cdot10^{-7}$, max. displacement=$6.0\cdot10^{-7}$), and an internally defined superfine grid size was used (SCF=tight, int=veryfinegrid), which is a pruned 175,974 grid for first-row atoms and a 250,974 grid for all other atoms. These parameters were chosen as recent literature indicated a significant dependence of the computed frequencies on the molecule orientation when a smaller grid size is used.[75] Geometries were optimized without symmetry constraints. All calculated stationary points have been verified by performing a vibrational analysis, to be energy minima (no imaginary frequencies) or transition states (only one imaginary frequency). The character of the normal mode associated with the imaginary frequency of the transition state has been analyzed to ensure that it is associated with the reaction of interest. Solvation in CH_2Cl_2 was taken into account in the computations using the PCM solvation model. Solvent effects were explicitly used in the solving of the SCF equations and during the optimization of the geometry and the vibrational analysis. The stationary point energies have been refined by performing single points at SMD(CH_2Cl_2)-(TightPNO)DLPNO-CCSD(T)/CBS(3,4/def2),[76–78] using ORCA 5.0.3,[79,80] on the PCM(CH_2Cl_2)-B3LYP/6-311G(d,p) geometries. The potential energy surfaces of the studied addition reactions were obtained by performing intrinsic reaction coordinate (IRC) calculations, which, in turn, were analyzed using the PyFrag program.[81] The optimized structures were illustrated using CYLview.[82]

The denoted free Gibbs energy was calculated using Equation S1, in which $\Delta E_{\text{dichloromethane}}$ is the solution-phase energy (electronic energy), $\Delta G_{\text{dichloromethane,QH}}$ (T = 213.15 K, C = 1 M standard state) is the sum of corrections from the electronic energy to the free Gibbs energy in the quasi-harmonic oscillator approximation, including zero-point-vibrational energy. The $\Delta G_{\text{gas,QH}}$ was computed using the quasi-harmonic approximation in the solution phase according to the work of Truhlar. The quasi-harmonic approximation is the same as the harmonic oscillator approximation except for those vibrational frequencies lower than 100 cm^{-1} were raised to 100 cm^{-1} as a way to correct for the breakdown of the harmonic oscillator model for the free energies of low-frequency vibrational modes.[83,84]

$$\Delta G_{\text{dichloromethane}} = \Delta E_{\text{dichloromethane}} + \Delta G_{\text{dichloromethane,QH}} \quad \text{(S1)}$$

Solution-phase Activation Strain

The activation strain model (ASM) analysis[53,54] and energy decomposition analysis (EDA)[55–57] were performed using the Amsterdam Density Functional (ADF2017.103)[85–87] software package based on the solution-phase structures obtained by Gaussian 09 rev D.01. For all computations, the B3LYP functional was used. The basis set used, denoted TZ2P, is of triple-ζ quality for all atoms and has been improved by two sets of polarization functions.[88] The accuracies of the fit scheme (Zlm fit) and the integration grid (Becke grid) were, for all calculations, set to VERYGOOD.[89,90] Relativistic effects were accounted for by using the zeroth-order regular approximation (ZORA).[91,92] All computations were performed in the gas-phase and with implicit solvation using COSMO.

The activation strain model (ASM) of chemical reactivity,[53,54] also known as the distortion/interaction model, is a fragment-based approach in which the (solution-phase) reaction profiles can be described with respect to, and understood in terms of the characteristics of, the reactants. It considers the rigidity of the reactants and to which extent they need to deform during the reaction, plus their capability to interact with each other as the reaction proceeds. With the help of this model the total energy, *i.e.*, $\Delta E_{\text{solution}}(\zeta)$, is decomposed into the strain and interaction energy, $\Delta E_{\text{solution-strain}}(\zeta)$ and $\Delta E_{\text{solution-int}}(\zeta)$, respectively, and project these values onto the reaction coordinate ζ [Eq. (S2)].

$$\Delta E_{\text{solution}}(\zeta) = \Delta E_{\text{solution-strain}}(\zeta) + \Delta E_{\text{solution-int}}(\zeta) \quad \text{(S2)}$$

In this equation, the strain energy, $\Delta E_{\text{solution-strain}}(\zeta)$, is the penalty that needs to be paid to deform the reactants from their equilibrium to the geometry they adopt during the reaction at the point ζ of the reaction coordinate. On the other hand, the interaction energy, $\Delta E_{\text{solution-int}}(\zeta)$, accounts for all the chemical interactions that occur between these two deformed reactants along the reaction coordinate. The total strain energy can, in turn, be further decomposed into the strain energies corresponding to the deformation of the cation, $\Delta E_{\text{solution-strain,cation}}(\zeta)$, as well as from the allyltrimethylsilane, $\Delta E_{\text{solution-strain,allyltrimethylsilane}}(\zeta)$ [Eq. S3].

$$\Delta E_{\text{solution-strain}}(\zeta) = \Delta E_{\text{solution-strain,cation}}(\zeta) + \Delta E_{\text{solution-strain,allyltrimethylsilane}}(\zeta) \quad \text{(S3)}$$

In order to further analyze the interaction energy, the solution-phase potential energy surface, *i.e.,* $\Delta E_{\text{solution}}(\zeta)$, was further decomposed into the $\Delta E_{\text{solvation}}(\zeta)$, which accounts for the interaction between the solute and solvent, and the $\Delta E_{\text{solute}}(\zeta)$, which is the reaction system in gas-phase with the solution-phase geometry [Eq. S4].[93]

$$\Delta E_{\text{solution}}(\zeta) = \Delta E_{\text{solvation}}(\zeta) + \Delta E_{\text{solute}}(\zeta) \quad \text{S4}$$

The solute term, $\Delta E_{\text{solute}}(\zeta)$, is subsequently decomposed into the solvent-free strain, $\Delta E_{\text{solute-strain}}(\zeta)$, and interaction energy, $\Delta E_{\text{solute-int}}(\zeta)$, which are referred to as solute strain and solute interaction, respectively, to distinguish between the two solution-phase activation strain schemes [Eq. S5].

$$\Delta E_{\text{solution}}(\zeta) = \Delta E_{\text{solvation}}(\zeta) + \Delta E_{\text{solute-strain}}(\zeta) + \Delta E_{\text{solute-int}}(\zeta) \quad \text{S5}$$

For clarity reasons, $\Delta E_{\text{solution}}$, $\Delta E_{\text{solution-strain}}$, $\Delta E_{\text{solution-int}}$, ΔE_{solute}, $\Delta E_{\text{solute-strain}}$, and $\Delta E_{\text{solute-int}}$ are denoted as ΔE, ΔE_{strain} and ΔE_{int} in all cases, however, one can easily deduce based on the level of theory if the ΔE_{solute} or $\Delta E_{\text{solution}}$ is decomposed.

In the herein presented activation strain and accompanied energy decomposition diagrams, the intrinsic reaction coordinate (IRC) is projected onto the carbon–leaving group (C•••Si) stretch. This critical reaction coordinate undergoes a well-defined change during the reaction from the reactant complex via the transition state to the product and is shown to be a valid reaction coordinate for studying bimolecular reactions. The ASM has been used to analyze the factors affecting the reaction paths of cycloaddition reactions, nucleophilic substitution reactions, eliminations reactions as well as epoxide opening reactions.[62,64,65,94,95]

Energy Decomposition Analysis

The interaction energy, *i.e.,* $\Delta E_{\text{solute-int}}(\zeta)$, between the deformed reactants can be further analyzed in terms of quantitative Kohn-Sham molecular orbital (KS-MO) theory together with a canonical energy decomposition analysis (EDA).[55–57] The EDA decomposes the $\Delta E_{\text{solute-int}}(\zeta)$ into the following three energy terms [Eq. (S6)]:

$$\Delta E_{\text{solute-int}}(\zeta) = \Delta V_{\text{elstat}}(\zeta) + \Delta E_{\text{Pauli}}(\zeta) + \Delta E_{\text{oi}}(\zeta) \quad \text{(S6)}$$

Herein, $\Delta V_{\text{elstat}}(\zeta)$ is the classical electrostatic interaction between the unperturbed charge distributions of the (deformed) reactants and is usually attractive. The Pauli repulsion, $\Delta E_{\text{Pauli}}(\zeta)$, includes the destabilizing interaction between the fully occupied orbitals of both fragments due to the Pauli principle. The orbital interaction energy, $\Delta E_{\text{oi}}(\zeta)$, accounts for, amongst others, charge transfer between the fragments, such as HOMO–LUMO interactions.

Estimation of Transition States

Establishing the transition state of reactions where a simple bond is formed to give one product or broken to give two fragments with minimal structural change is fundamentally difficult (*i.e.*, dissociation and association transition states). To find transition states, the potential energy surface (PES) is scanned for a saddle point, and specifically, the electronic energy surface. Very simple bond cleavage events are often not associated with such a saddle point on the electronic energy surface, which makes it impossible to locate these transition states. This scenario was also found in selected cases for the S_E2' reactions studied here. To provide an accurate approximation of the transition state in these cases, the Gibbs potential energy surface was computed and considered, as commonly done in variational transition state theory when barrierless reactions are studied,[96–98] the first high-order saddle point upon elongation of the C-1•••allyltrimethylsilane bond (started from the product complex) as an estimation of the transition.

The Gibbs potential energy surface was determined from a relaxed potential energy surface scan using Gaussian 09 rev D.01, at PCM(CH_2Cl_2)-B3LYP/6-311G(d,p) utilizing the keywords: opt=tight, SCF=tight, int=veryfinegrid. First, the electronic relaxed potential energy surface was constructed. The starting point of each scan was the product complex. From here, the C-1•••allyltrimethylsilane bond was elongated in 100 steps with a fine step size of 0.025 Å, while allowing the rest of the geometry to optimize. The Gibbs relaxed potential energy surface was then constructed by computing the vibrational frequencies for each point.

To verify the viability of this approach, the transition state was approximated for the top face attack on the $^3H_4$ and the bottom face attack on the $^4H_3$ for all the studied cations (**1**, **2**, **3**, **4**, **5** and **6**), for which the transition states (except the top face attack of cation **2**) could be located (see Table S3 and Table S4). The $\Delta G^{\ddagger *}$ of the approximated transition states were very close to the $\Delta G^{\ddagger}$ of the corresponding TS (average deviation = 0.16 kcal mol^{-1}, RMSD = 0.20 kcal mol^{-1}), supporting this method for estimating the transition state.

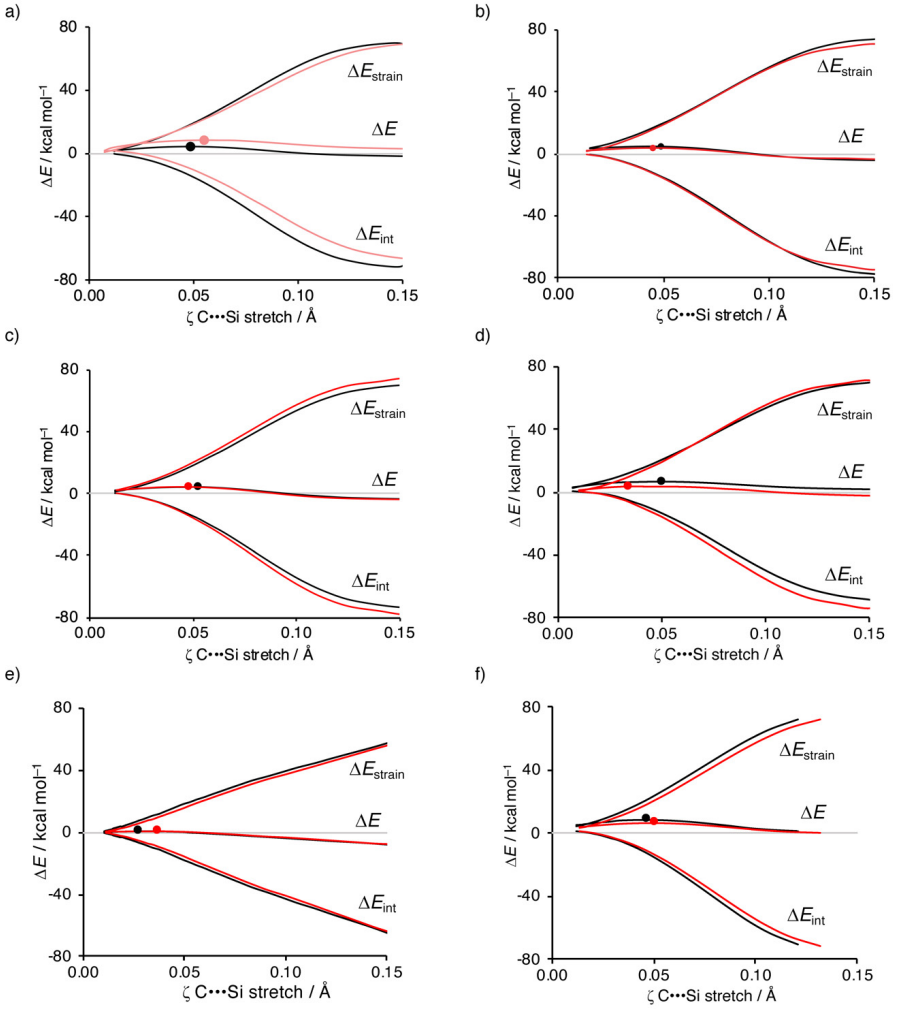

Figure S1. Activation strain model for the S_E2' reactions of allyltrimethylsilane + cation **1** (a) via the top face-attack (black: chair-like TS) and bottom face-attack (pink: twist boat-like TS), and **4** (b), **3** (c), **5** (d), **2** (e), **6** (f) via the top face-attack (black: chair-like TS) and bottom face-attack (red: chair-like TS), where the energy values are plotted along the IRC projected on the C•••Si bond stretch. Computed at COSMO(CH_2Cl_2)-ZORA-B3LYP/TZ2P//PCM(CH_2Cl_2)-B3LYP/6-311G(d,p).

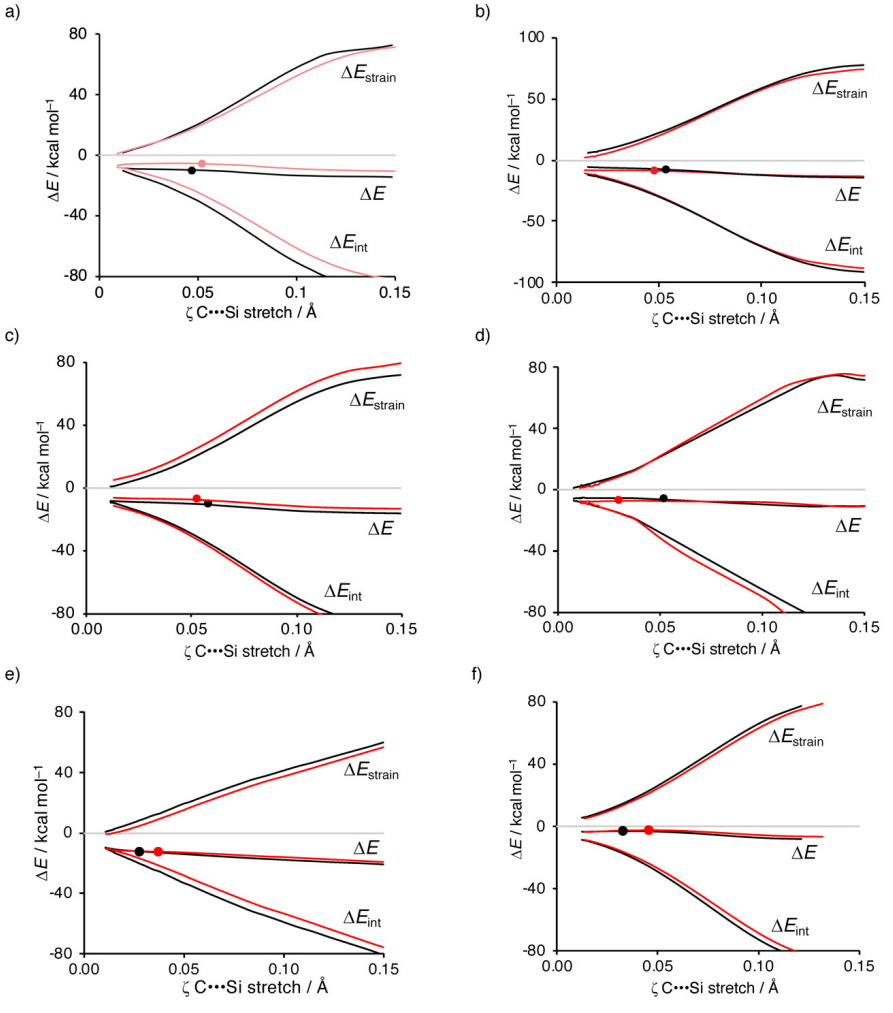

Figure S2. Activation strain model for the S_E2' reactions of allyltrimethylsilane + cation **1** (a) via the top face-attack (black; chair-like TS) and bottom face-attack (pink; twist boat-like TS), and **4** (b), **3** (c), **5** (d), **2** (e), **6** (f) via the top face-attack (black; chair-like TS) and bottom face-attack (red; chair-like TS), where the energy values are plotted along the IRC projected on the C•••Si bond stretch. Computed at ZORA-B3LYP/TZ2P//PCM(CH_2Cl_2)-B3LYP/6-311G(d,p).

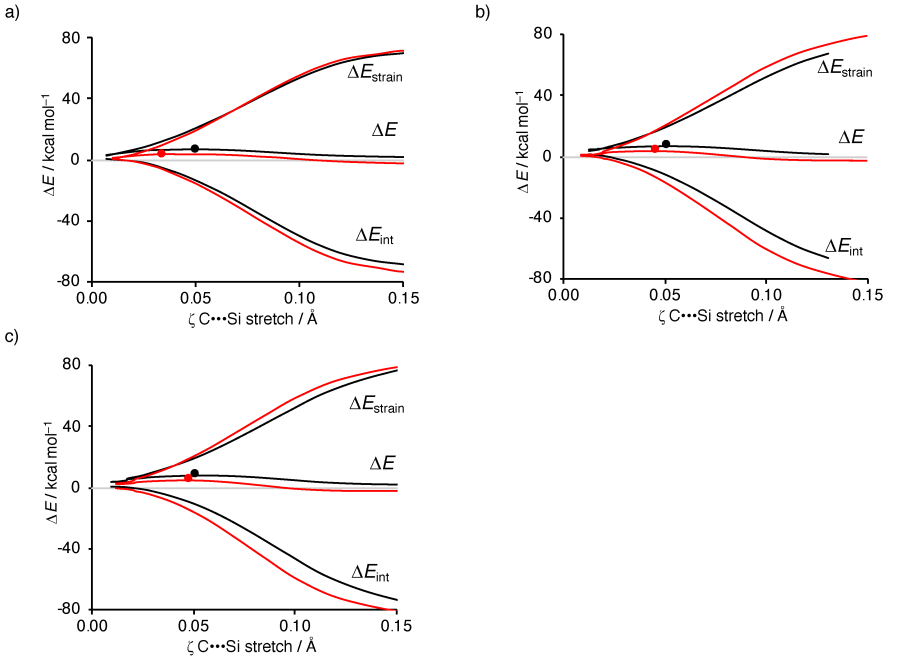

Figure S3. Activation strain model for the S_E2' reactions of allyltrimethylsilane + cation **5** with *gg* rotamer (a), *gt* rotamer (b), *tg* rotamer (c) via the top face-attack (black: chair-like TS) and bottom face-attack (red: chair-like TS), where the energy values are plotted along the IRC projected on the C•••Si bond stretch. Computed at COSMO(CH_2Cl_2)-ZORA-B3LYP/TZ2P//PCM(CH_2Cl_2)-B3LYP/6-311G(d,p).

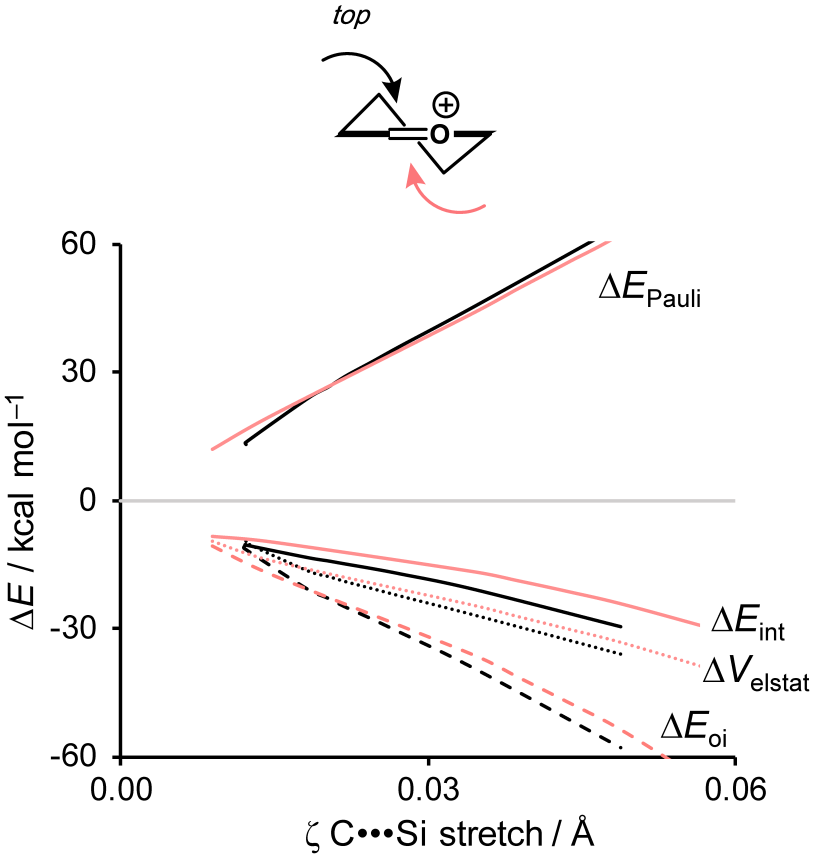

Figure S4. Energy decomposition analysis for the S_E2' reactions of allyltrimethylsilane and cation **1** via the top face-attack (black: chair-like TS) and bottom face-attack (pink: twist boat-like TS), where the energy values are plotted to the transition state (indicated by a dot), along the IRC projected on the C•••Si bond stretch.

Pyramidalization

Figure S5a illustrates that the pyramidalization is directly coupled to the C–O stretch (*i.e.*, C1=O$^+$ bond). A larger degree of C1-pyramidalization (*i.e.*, sp^2 to sp^3 rehybridization) of the cation results in a longer C1=O$^+$ bond. Figure S5b and S5c reinforces that the chair-like TS (black) pathway has a significantly larger degree of pyramidalization than the twist boat-like TS (red) at the same C•••Si bond stretch.

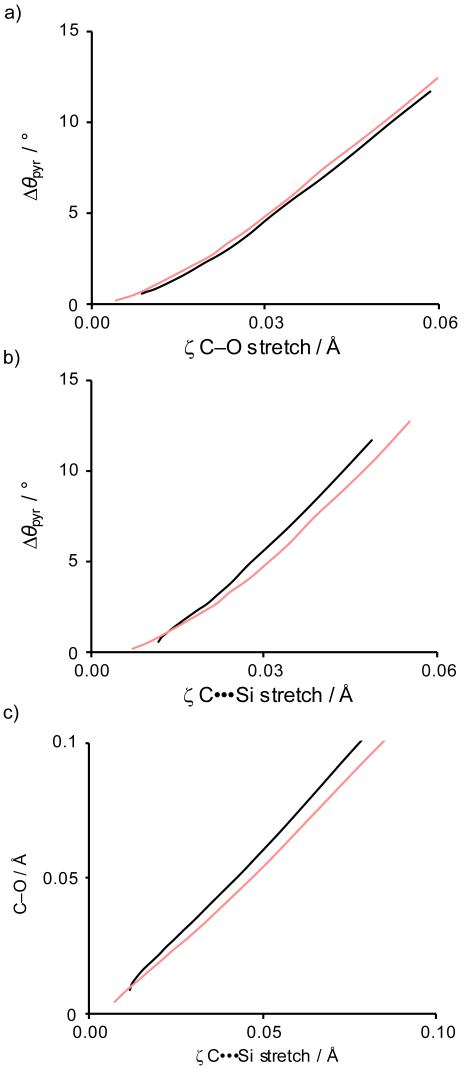

Figure S5. Degree of pyramidalization for the S_E2' reactions of allyltrimethylsilane and cation **1** via the top face-attack (black: chair-like TS) and bottom face-attack (pink: twist boat-like TS), where the energy values are plotted from the reactant complex to the transition state, along the IRC projected on the (a) C–O (b) C•••Si bond stretch. The pyramidalization angle is defined as the sum of the three θ_{R-C1-R}. Computed at COSMO(CH_2Cl_2)-ZORA-B3LYP/TZ2P//PCM(CH_2Cl_2)-B3LYP/6-311G(d,p).

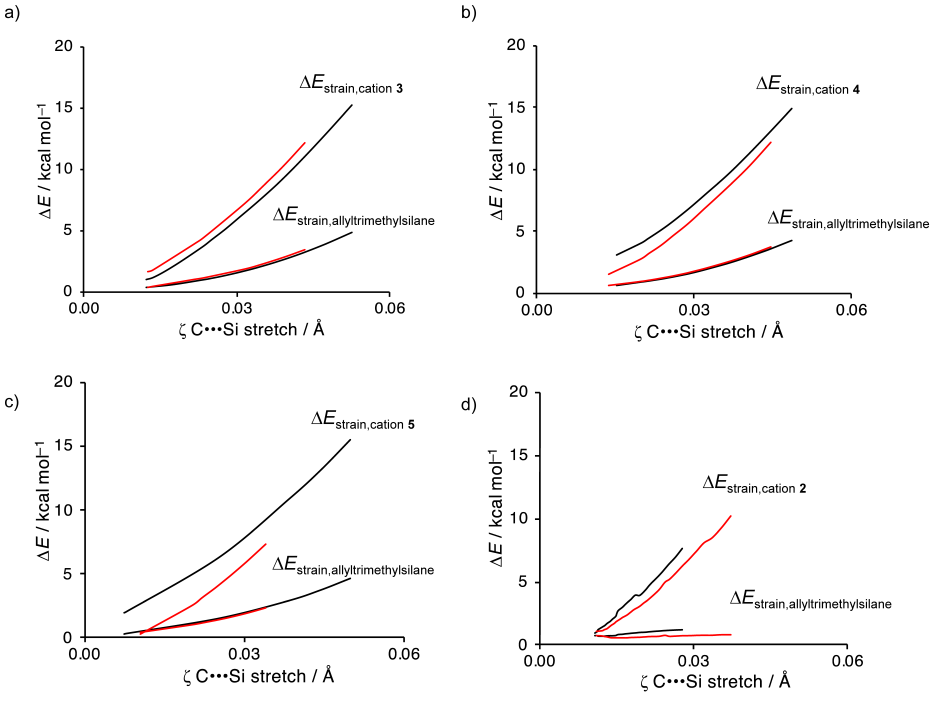

Figure S6. Strain decomposition for the S_E2' reactions of allyltrimethylsilane + cation **3** (a), **4** (b), **5** (c), and **2** (d) via the top face-attack (black: chair-like TS) and bottom face-attack (red: chair-like TS), where the energy values are plotted along the IRC projected on the C•••Si bond stretch. Computed at COSMO(CH_2Cl_2)-ZORA-B3LYP/TZ2P//PCM(CH_2Cl_2)-B3LYP/6-311G(d,p).

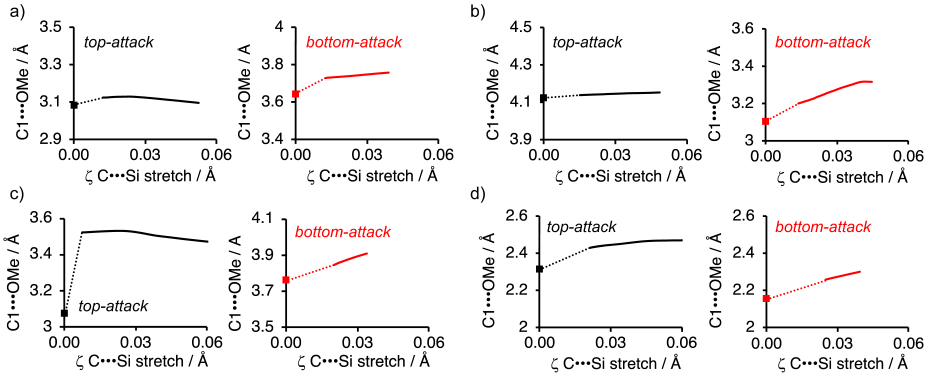

Figure S7. Distance plot with this length between the electrophilic *C*-atom of the C1-postition and *O*-atom of the substituent in Å (equilibrium geometry is indicated with a box) projected onto the C•••Si bond stretch for the S_E2' reactions of allyltrimethylsilane + **3** (a), **4** (b), **5** (c), and **2** (d) via the top-attack (black: chair-like TS) and bottom-attack (red: chair-like TS).

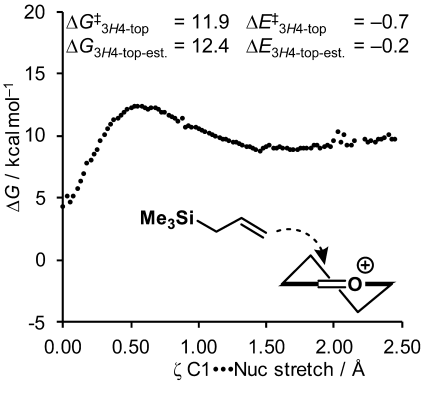

Figure S8. Potential Gibbs energy surface (see Computation Methods for details) scan of the S_E2' reactions of allyltrimethylsilane + **1** via the top-attack (chair-like TS). Computed at PCM(CH_2Cl_2)-B3LYP/6-311G(d,p).

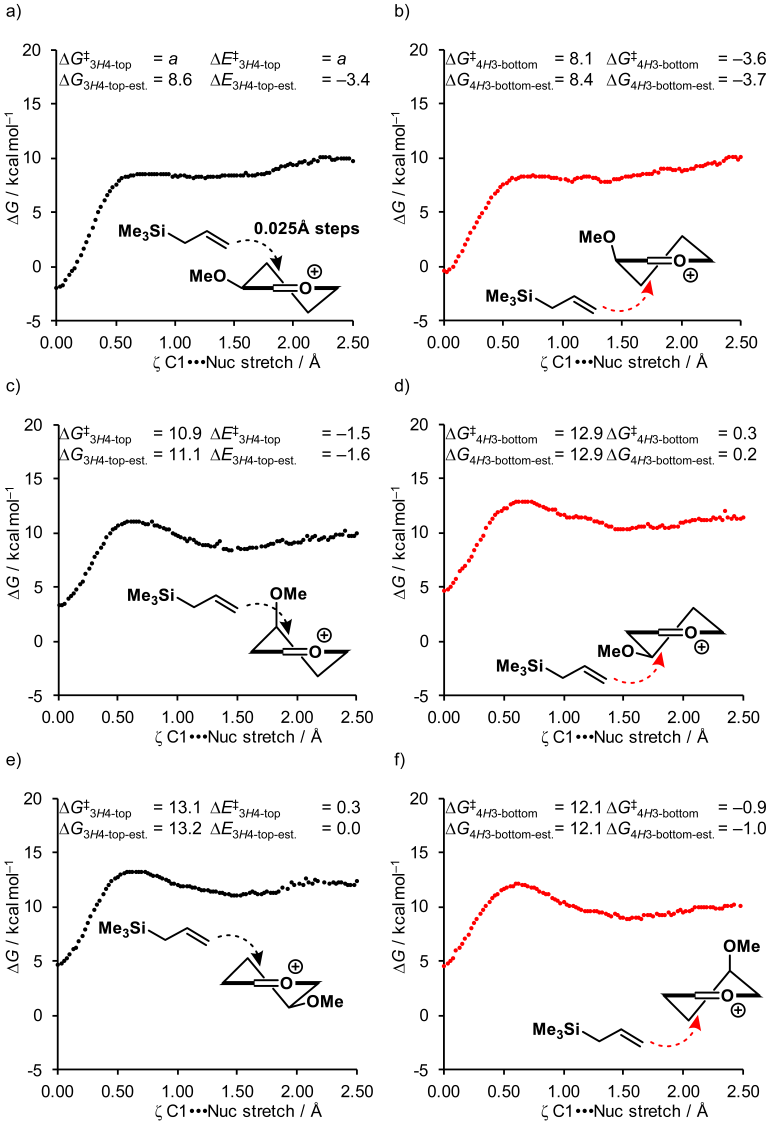

Figure S9. Potential Gibbs energy surface scan (see Computation Methods for details) of the S_E2' reactions of allyltrimethylsilane + **2** (a, b), **3** (c, d) and **4** (e, f) via the top-attack (black: $^1C_4$-like TS) (a, c and e) and the bottom-attack (red: $^4C_1$-like TS) (b, d and f). Computed at PCM(CH_2Cl_2)-B3LYP/6-311G(d,p).

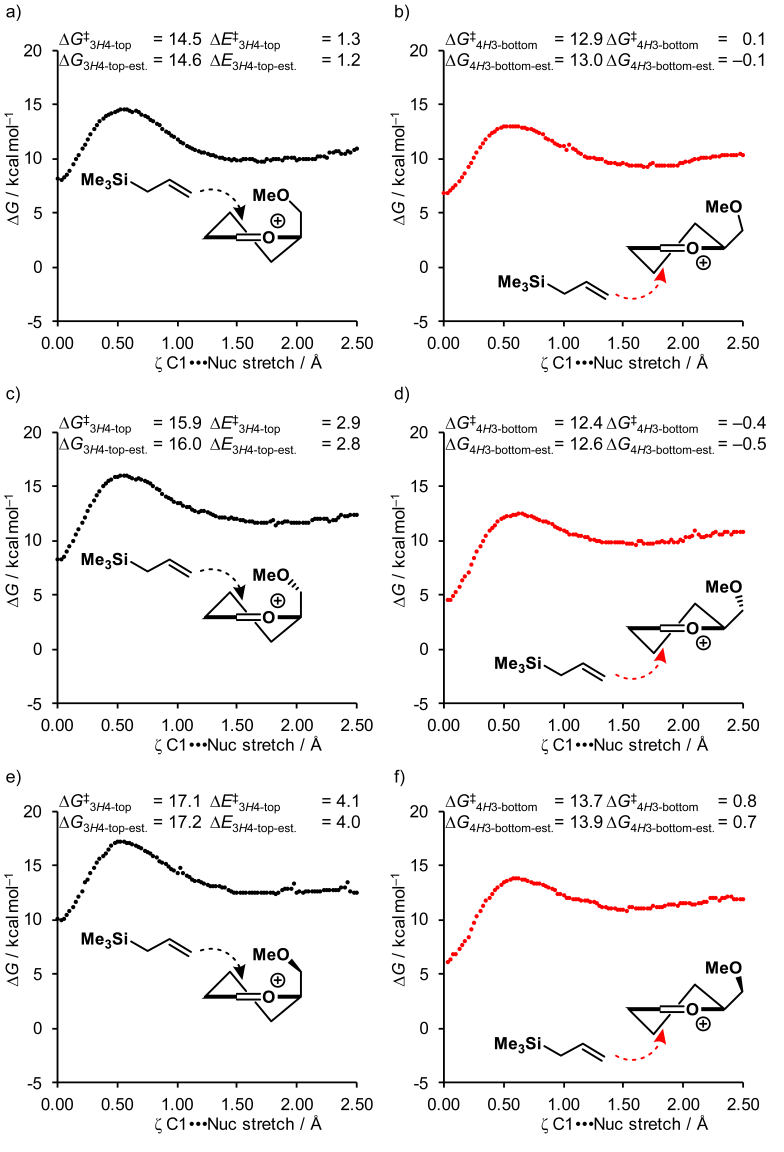

Figure S10. Potential Gibbs energy surface scan (see Computation Methods for details) of the S_E2' reactions of allyltrimethylsilane + **5** via the top-attack (black: $^1C_4$-like TS) (a, c and e) and the bottom-attack (red: $^4C_1$-like TS) (b, d, f). All three rotamers were plotted: *gg* (a and b), *gt* (c and d) and *tg* (e and f). Computed at PCM(CH_2Cl_2)-B3LYP/6-311G(d,p).

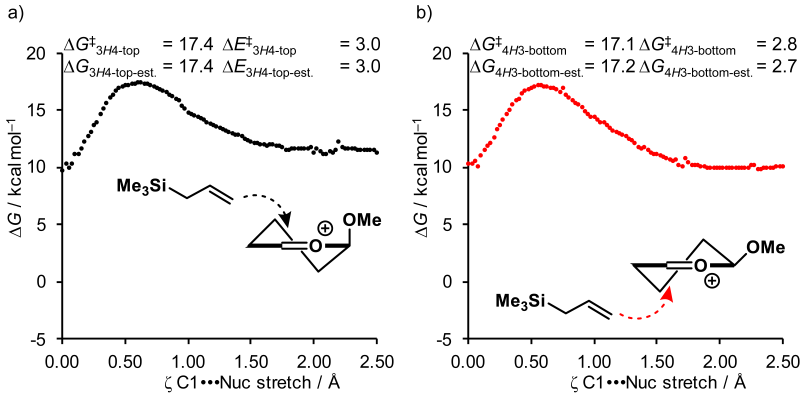

Figure S11. Potential Gibbs energy surface scan (see Computation Methods for details) of the S_E2' reactions of allyltrimethylsilane + **6** via the top-attack (black: $^1C_4$-like TS) (a) and the bottom-attack (red: $^4C_1$-like TS) (b). Computed at PCM(CH_2Cl_2)-B3LYP/6-311G(d,p). **Table S1.** PCM(CH_2Cl_2)-B3LYP/6-311G(d,p) Gibbs energies (ΔG_{DCM}, in kcal mol^{-1}) and in parentheses electronic energies (ΔE_{DCM}, in kcal mol^{-1}) in dichloromethane relative to reactants of the stationary points of the S_E2' reaction between allyltrimethylsilane and oxocarbenium ions **1**-**6**. All energies (R, TS and P) are reported relative to the lowest energy conformer.

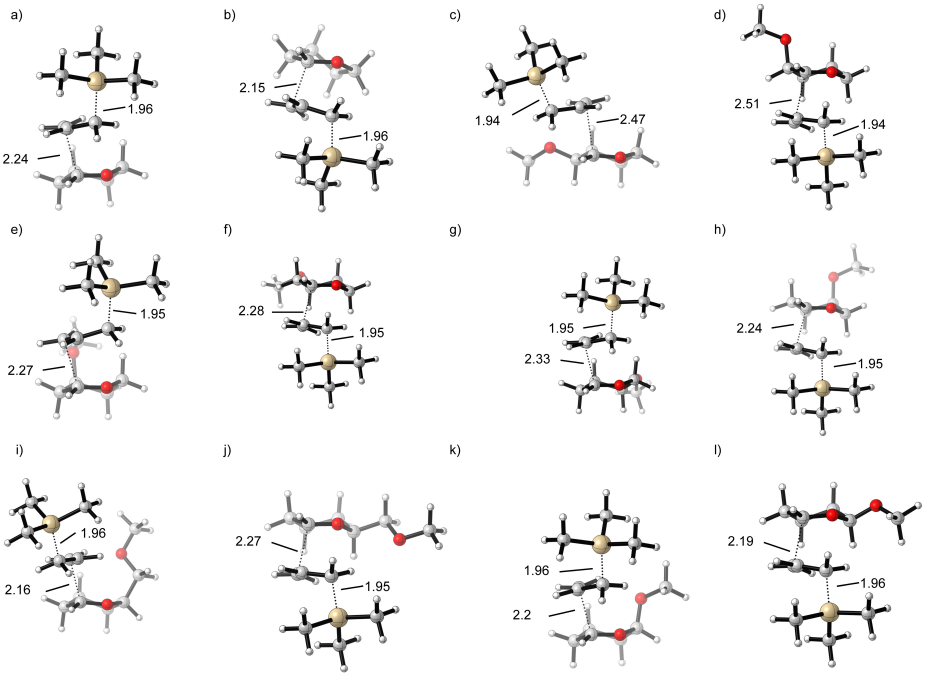

Figure S12. Structures[82] of the critical transition state geometries with key distances (in Å). The S_E2' reactions of allyltrimethylsilane + **1** via the top $^1C_4$-like TS (a), **1** via the bottom $^5S_5$-like TS (b), **2** via the top $^1C_4$-like TS (c), **2** via the bottom $^4C_1$-like TS (d), **3** via the top $^1C_4$-like TS (e), **3** via the bottom $^4C_1$-like TS (f), **4** via the top $^1C_4$-like TS (g), **4** via the bottom $^4C_1$-like TS (h), **5** via the top $^1C_4$-like TS (i), **5** via the bottom $^4C_1$-like TS (j), **6** via the top $^1C_4$-like TS (k), **6** via the bottom $^4C_1$-like TS (l).

Table S1. PCM(CH_2Cl_2)-B3LYP/6-311G(d,p) Gibbs energies (ΔG_{DCM}, in kcal mol^{-1}) and in parentheses electronic energies (ΔE_{DCM}, in kcal mol^{-1}) in CH_2Cl_2 relative to reactants of the stationary points of the S_E2' reaction between allyltrimethylsilane and oxocarbenium ions **1**-**6**. All energies (R, RC, TS, PC and P) are reported relative to the lowest energy conformer.[61,99]

species	**1**	**2**	**3**	**4**	**5-*gg***	**5-*gt***	**5-*tg***	**6**
$^3H_4$-R	0.0 (0.0)	0.0 (0.3)	0.0 (0.0)	2.0 (2.3)	0.4 (0.1)	2.9 (2.7)	2.2 (2.3)	1.1 (1.0)
$^4H_3$-R	[a]	0.1 (0.0)	1.1 (1.4)	0.0 (0.0)	0.0 (0.0)	1.7 (1.9)	0.5 (0.9)	0.0 (0.0)
$^3H_4$-RC-top	9.0 (−2.2)	9.2 (−1.9)	8.8 (−2.6)	11.4 (−0.6)	9.9 (−1.7)	11.9 (−0.1)	12.5 (0.8)	12.0 (−0.1)
$^3H_4$-RC-bottom	9.3 (−1.5)	9.3 (−2.0)	10.3 (−1.3)	11.9 (0.5)	10.2 (−1.2)	12.4 (1.2)	13.1 (1.3)	11.7 (0.2)
$^4H_3$-RC-top	[a]	9.4 (−1.8)	10.5 (−0.7)	9.2 (−2.0)	9.5 (−2.2)	11.7 (0.5)	11.2 (−0.6)	10.7 (−0.9)
$^4H_3$-RC-bottom	[a]	8.2 (−3.7)	10.7 (−0.9)	9.4 (−2.5)	9.6 (−2.2)	9.9 (−1.8)	11.1 (−0.5)	10.2 (−0.8)
$^{2,5}B$-TS	5.1 (4.9)	5.4 (5.6)	6.0 (6.1)	5.8 (5.4)	4.8 (4.4)	8.7 (8.4)	7.5 (7.5)	7.7 (6.7)
$B_{2,5}$-TS	[a]	2.8 (3.0)	4.4 (4.2)	6.0 (5.8)	5.3 (4.7)	7.1 (6.8)	5.7 (5.5)	6.3 (5.6)
$^3H_4$-TS-top-C	11.9 (−0.7)	[b]	10.9 (−1.5)	13.1 (0.3)	14.5 (1.3)	15.9 (2.9)	17.1 (4.1)	17.4 (3.0)
$^3H_4$-TS-bottom-TB	16.2 (3.5)	11.7 (−0.8)	16.0 (3.3)	15.0 (2.2)	15.9 (2.8)	16.7 (3.7)	14.1 (1.5)	19.2 (4.9)
$^4H_3$-TS-top-TB	[a]	10.9 (−1.4)	14.5 (1.9)	14.2 (1.3)	16.3 (2.7)	18.4 (5.3)	17.2 (3.9)	20.1 (6.1)
$^4H_3$-TS-bottom-C	[a]	8.1 (−3.6)	12.9 (0.3)	12.1 (−0.9)	12.9 (0.1)	12.4 (−0.4)	13.7 (0.8)	17.1 (2.8)
$^3H_4$-PC-top	4.4 (−10.0)	−1.9 (−16.3)	3.3 (−11.5)	4.7 (−10.4)	8.2 (−7.2)	8.3 (−6.5)	10.1 (−4.9)	9.7 (−7.0)
$^3H_4$-PC-bottom	6.7 (−7.2)	3.6 (−10.5)	6.6 (−7.9)	6.0 (−8.6)	8.5 (−6.2)	8.1 (−6.3)	5.8 (−9.1)	11.5 (−4.8)
$^4H_3$-PC-top	[a]	2.4 (−11.6)	7.8 (−6.8)	7.5 (−7.9)	9.7 (−5.5)	2.8 (−12.0)	9.8 (−5.4)	10.3 (−6.5)
$^4H_3$-PC-bottom	[a]	−0.4 (−14.8)	4.7 (−10.0)	4.6 (−10.0)	6.9 (−8.3)	4.7 (−10.6)	6.0 (−8.8)	15.2 (−1.2)
$^3H_4$-P-top	−35.1 (−48.5)	−41.4 (−54.6)	−35.8 (−49.4)	−36.0 (−49.7)	−30.0 (−43.9)	−30.3 (−44.0)	−29.9 (−44.0)	−30.4 (−45.8)
$^3H_4$-P-bottom	−32.0 (−45.1)	−38.7 (−51.5)	−32.6 (−45.8)	−11.5 (−47.1)	−30.9 (−44.3)	−28.2 (−41.6)	−31.5 (−44.8)	−28.2 (−43.1)
$^4H_3$-P-top	[a]	−36.1 (−48.9)	−31.3 (−44.8)	−33.7 (−47.4)	−28.7 (−42.4)	−28.2 (−41.6)	−27.7 (−41.4)	−26.1 (−41.1)
$^4H_3$-P-bottom	[a]	−40.9 (−54.1)	−36.1 (−49.5)	−35.4 (−49.2)	−33.8 (−47.5)	−34.5 (−48.1)	−33.7) (−47.4)	−31.0 (−46.2)

[a] For the unsubstituted oxocarbenium ion **1**, the computed values are only depicted for the $^3H_4$, since both the $^3H_4$ and $^4H_3$ are chemically equivalent. [b] Nonexistent: barrierless process toward the product (see Table S3). R = reactant, RC = reactant complex, TS = transition state, C = chair-like, TB = twist boat-like, PC = product complex and P = product.

Table S2. SMD(CH_2Cl_2)-(TightPNO)DLPNO-CCSD(T)/CBS(3,4/def2)//PCM(CH_2Cl_2)-B3LYP/6-311G(d,p) Gibbs energies (ΔG_{DCM}, in kcal mol^{-1}) and in parentheses electronic energies (ΔE_{DCM}, in kcal mol^{-1}) in CH_2Cl_2 relative to reactants of the stationary points of the S_E2' reaction between allyltrimethylsilane and oxocarbenium ions **1**-**6**. All energies (R, RC, TS, PC and P) are reported relative to the lowest energy conformer.[61,99]

species	**1**	**2**	**3**	**4**	**5-*gg***	**5-*gt***	**5-*tg***	**6**
$^3H_4$-R	0.0 (0.0)	0.0 (0.0)	0.0 (0.0)	2.2 (2.4)	1.0 (0.7)	2.6 (2.4)	1.2 (1.4)	1.0 (0.9)
$^4H_3$-R	[a]	0.9 (0.6)	0.6 (0.9)	0.0 (0.0)	0.0 (0.0)	1.6 (1.9)	0.0 (0.3	0.0 (0.0)
$^3H_4$-RC-top	7.4 (–3.8)	7.4 (–4.0)	7.4 (–4.0)	9.9 (–2.0)	9.2 (–2.4)	9.0 (–3.0)	10.3 (–1.3)	7.6 (–4.6)
$^3H_4$-RC-bottom	7.4 (–3.4)	7.4 (–4.2)	8.0 (–3.6)	10.2 (–1.2)	8.8 (–2.6)	10.2 (–1.0)	10.5 (–1.4)	7.8 (–3.7)
$^4H_3$-RC-top	[a]	7.7 (–3.7)	8.3 (–3.0)	7.6 (–3.6)	7.2 (–4.4)	9.5 (–1.6)	8.2 (–3.6)	7.0 (–4.7)
$^4H_3$-RC-bottom	[a]	7.4 (–4.7)	8.3 (–3.3)	7.6 (–4.3)	7.6 (–4.2)	7.3 (–4.4)	9.0 (–2.6)	8.0 (–3.0)
$^{2,5}B$-TS	4.9 (4.7)	5.4 (5.3)	5.9 (6.1)	5.5 (5.1)	5.6 (5.2)	8.0 (7.8)	6.1 (6.0)	5.4 (4.4)
$B_{2,5}$-TS	[a]	2.3 (2.3)	3.4 (3.2)	6.0 (5.8)	5.0 (4.4)	6.7 (6.4)	4.9 (4.7)	4.4 (3.7)
$^3H_4$-TS-top-C	11.3 (–1.3)	[b]	11.3 (–1.1)	12.8 (–0.1)	15.6 (2.3)	14.7 (1.8)	16.6 (3.5)	12.1 (–2.3)
$^3H_4$-TS-bottom-TB	16.5 (3.8)	11.0 (–1.7)	16.1 (3.4)	14.0 (1.2)	14.9 (1.8)	15.6 (2.7)	12.5 (–0.1)	13.9 (–0.4)
$^4H_3$-TS-top-TB	[a]	10.6 (–2.0)	14.5 (1.9)	15.7 (2.7)	16.6 (3.0)	17.8 (4.7)	16.2 (2.9)	15.1 (1.1)
$^4H_3$-TS-bottom-C	[a]	7.3 (–4.7)	11.7 (–0.9)	11.5 (–1.5)	11.8 (–1.0)	11.2 (–1.7)	12.7 (–0.2)	11.3 (–3.0)
$^3H_4$-PC-top	–1.9 (–16.3)	–8.5 (–23.1)	–3.2 (–18.1)	–2.2 (–17.2)	3.0 (–12.4)	1.3 (–13.5)	2.6 (–12.4)	–3.1 (–19.9)
$^3H_4$-PC-bottom	0.3 (–13.7)	–4.4 (–18.8)	0.5 (–14.0)	–0.6 (–15.2)	1.9 (–12.8)	0.9 (–13.6)	–0.6 (–15.5)	–0.3 (–16.6)
$^4H_3$-PC-top	[a]	–4.4 (–18.6)	2.0 (–12.6)	1.6 (–13.8)	4.0 (–11.1)	–4.4 (–19.1)	2.5 (–12.7)	–3.1 (–19.9)
$^4H_3$-PC-bottom	[a]	–7.9 (–22.5)	–3.2 (–17.8)	–2.0 (–16.6)	–0.3 (–15.4)	–1.8 (–17.1)	–1.5 (–16.3)	3.4 (–13.0)
$^3H_4$-P-top	–36.2 (–49.6)	–43.8 (–57.3)	–37.0 (–50.5)	–37.4 (–51.2)	–30.4 (–44.3)	–32.0 (–45.7)	–31.7 (–45.8)	–37.0 (–52.4)
$^3H_4$-P-bottom	–33.6 (–46.6)	–40.8 (–53.9)	–34.2 (–47.4)	–13.0 (–48.6)	–32.8 (–46.2)	–30.3 (–43.7)	–33.9 (–47.3)	–35.3 (–50.2)
$^4H_3$-P-top	[a]	–38.1 (–51.2)	–32.2 (–45.8)	–34.7 (–48.4)	–29.5 (–43.2)	–30.3 (–43.7)	–29.7 (–43.5)	–32.5 (–47.5)
$^4H_3$-P-bottom	[a]	–43.4 (–56.8)	–38.2 (–51.6)	–36.9 (–50.7)	–35.9 (–49.6)	–36.5 (–50.1)	–36.5 (–50.2)	–38.2 (–53.4)

[a] For the unsubstituted oxocarbenium ion **1**, the computed values are only depicted for the $^3H_4$, since both the $^3H_4$ and $^4H_3$ are chemically equivalent. [b] Nonexistent: barrierless process toward the product (see Table S4). R = reactant, RC = reactant complex, TS = transition state, C = chair-like, TB = twist boat-like, PC = product complex and P = product.

Table S3. PCM(CH_2Cl_2)-B3LYP-D3(BJ)/6-311G(d,p)//PCM(CH_2Cl_2)-B3LYP/6-311G(d,p) Gibbs energies (ΔG_{DCM}, in kcal mol^{-1}) and in parentheses electronic energies (ΔE_{DCM}, in kcal mol^{-1}) in CH_2Cl_2 relative to reactants of the stationary points of the S_E2' reaction between allyltrimethylsilane and oxocarbenium ions **1**-**6**. All energies (R, RC, TS, PC and P) are reported relative to the lowest energy conformer. [61,99]

species	**1**	**2**	**3**	**4**	**5-*gg***	**5-*gt***	**5-*tg***	**6**
$^3H_4$-R	0.0 (0.0)	0.0 (0.5)	0.0 (0.0)	2.4 (2.7)	–0.4 (–0.8)	2.5 (2.3)	2.0 (2.1)	0.9 (0.8)
$^4H_3$-R	[a]	–0.2 (0.0)	1.4 (1.8)	0.0 (0.0)	0.0 (0.0)	1.8 (2.1)	0.8 (1.1)	0.0 (0.0)
$^3H_4$-RC-top	4.7 (–6.5)	3.5 (–7.4)	3.4 (–8.0)	6.6 (–5.3)	4.8 (–6.8)	6.2 (–5.8)	7.7 (–4.0)	7.8 (–4.3)
$^3H_4$-RC-bottom	5.3 (–5.5)	4.4 (–6.8)	6.2 (–5.4)	8.1 (–3.4)	5.5 (–5.9)	8.1 (–3.1)	7.6 (–4.3)	7.8 (–3.7)
$^4H_3$-RC-top	[a]	2.9 –(8.1)	6.3 (–4.9)	4.3 (–6.9)	3.7 (–7.9)	7.6 (–3.6)	6.7 (–5.1)	7.1 (–4.5)
$^4H_3$-RC-bottom	[a]	2.0 –(9.6)	5.9 (–5.7)	4.3 (–7.5)	4.9 (–6.8)	4.9 (–6.8)	6.1 (–5.4)	7.0 (–4.0)
$^{2,5}B$-TS	5.1 (4.9)	5.1 (5.5)	6.4 (6.6)	6.1 (5.7)	3.9 (3.5)	8.3 (8.0)	7.2 (7.1)	7.7 (6.6)
$B_{2,5}$-TS	[a]	2.8 (3.3)	4.6 (4.4)	6.3 (6.1)	5.2 (4.7)	7.2 (6.9)	5.9 (5.7)	6.7 (6.0)
$^3H_4$-TS-top-C	4.8 (–7.7)	[b]	3.6 (–8.8)	6.5 (–6.4)	6.3 (–6.9)	7.5 (–5.5)	9.7 (–3.3)	9.2 (–5.2)
$^3H_4$-TS-bottom-TB	9.6 (–3.1)	4.4 (–7.8)	9.5 (–3.2)	9.1 (–3.7)	9.2 (–3.9)	10.1 (–2.8)	6.7 (–6.0)	11.6 (–2.8)
$^4H_3$-TS-top-TB	[a]	3.3 (–8.8)	7.0 (–5.6)	6.8 (–6.2)	7.2 (–6.4)	11.8 (–1.3)	9.6 (–3.8)	13.4 (–0.7)
$^4H_3$-TS-bottom-C	[a]	1.3 (–10.2)	6.1 (–6.5)	5.1 (–7.9)	5.7 (–7.2)	4.8 (–8.0)	6.5 (–6.4)	9.9 (–4.4)
$^3H_4$-PC-top	–2.4 (–16.8)	–9.1 (–23.3)	–4.0 (–18.9)	–2.2 (–17.2)	–0.9 (–16.2)	–0.7 (–15.6)	2.0 (–13.0)	1.5 (–15.3)
$^3H_4$-PC-bottom	0.3 (–13.6)	–3.9 (–17.8)	0.2 (–14.2)	–0.1 (–14.7)	1.8 (–12.8)	1.4 (–13.1)	–2.7 (–17.6)	4.2 (–12.1)
$^4H_3$-PC-top	[a]	–4.9 (–18.7)	0.0 (–14.5)	–0.1 (–15.5)	0.5 (–14.7)	–3.1 (–17.9)	0.3 (–14.9)	2.9 (–13.9)
$^4H_3$-PC-bottom	[a]	–7.9 (–22.0)	–1.9 (–16.6)	–2.4 (–17.0)	–0.5 (–15.6)	–4.3 (–19.6)	–1.2 (–16.1)	8.4 (–8.0)
$^3H_4$-P-top	–41.0 (–54.5)	–48.2 (–61.2)	–42.1 (–55.7)	–41.8 (–55.6)	–37.4 (–51.4)	–37.2 (–51.0)	–37.4 (–51.5)	–37.5 (–52.9)
$^3H_4$-P-bottom	–37.5 (–50.6)	–44.7 (–57.2)	–38.0 (–51.2)	–16.7 (–52.3)	–36.6 (–50.0)	–34.7 (–48.1)	–37.3 (–50.6)	–34.0 (–48.9)
$^4H_3$-P-top	[a]	–42.4 (–55.0)	–37.5 (–51.1)	–39.0 (–52.7)	–35.8 (–49.5)	–34.7 (–48.1)	–34.4 (–48.2)	–32.0 (–47.0)
$^4H_3$-P-bottom	[a]	–47.5 (–60.4)	–41.9 (–55.4)	–41.5 (–55.3)	–40.0 (–53.7)	–40.7 (–54.3)	–40.0 (–53.6)	–37.3 (–52.5)

[a] For the unsubstituted oxocarbenium ion **1**, the computed values are only depicted for the $^3H_4$, since both the $^3H_4$ and $^4H_3$ are chemically equivalent. [b] Nonexistent: barrierless process toward the product (see Table S3). R = reactant, RC = reactant complex, TS = transition state, C = chair-like, TB = twist boat-like, PC = product complex and P = product.

Table S4. PCM(CH_2Cl_2)-B3LYP/6-311G(d,p) Gibbs energies (ΔG_{DCM}, in kcal mol^{-1}) and in parentheses electronic energies (ΔE_{DCM}, in kcal mol^{-1}) in CH_2Cl_2 relative to reactants of the transition state stationary points and the estimated (based on PES scans) transition state of the S_E2' reaction between allyltrimethylsilane and oxocarbenium ions **1**-**6**. All energies (TS and TS Est.) are reported relative to the lowest energy conformer.[61,99]

species	**1**	**2**	**3**	**4**	**5-*gg***	**5-*gt***	**5-*tg***	**6**
$^3H_4$-TS-top-C	11.9	[c]	10.9	13.1	14.5	15.9	17.1	17.4
	(–0.7)	[c]	(–1.5)	(0.3)	(1.3)	(2.9)	(4.1)	(3.0)
$^3H_4$-TS-top-C	12.4	8.6	11.1	13.2	14.6	16.0	17.2	17.4
Est.[b]	(–0.2)	(–3.4)	(–1.6)	(0.0)	(1.2)	(2.8)	(4.0)	(3.0)
$^4H_3$-TS-bottom-C	[a]	8.1	12.9	12.1	12.9	12.4	13.7	17.1
	[a]	(–3.6)	(0.3)	(–0.9)	(0.1)	(–0.4)	(0.8)	(2.8)
$^4H_3$-TS-bottom-C	[a]	8.4	12.9	12.1	13.0	12.6	13.9	17.2
Est.[b]	[a]	(–3.7)	(0.2)	(-1.0)	(–0.1)	(–0.5)	(0.7)	(2.7)

[a] For the unsubstituted oxocarbenium ion **1**, the computed values are only depicted for the $^3H_4$, since both the $^3H_4$ and $^4H_3$ are chemically equivalent. [b] Estimated energies of TSs were obtained by performing frequency analysis of all non-stationary points of a relaxed PES scan, starting from the PC of which the C1•••Nuc bond was elongated in 100 steps of 0.025Å. [c] Nonexistent: barrierless process toward the product. TS = transition state, C = chair-like.

Table S5. SMD(CH_2Cl_2)-(TightPNO)DLPNO-CCSD(T)/CBS(3,4/def2)//PCM(CH_2Cl_2)-B3LYP/6-311G(d,p) Gibbs energies (ΔG_{DCM}, in kcal mol^{-1}) and in parentheses electronic energies (ΔE_{DCM}, in kcal mol^{-1}) in CH_2Cl_2 relative to reactants of the transition state stationary points and the estimated (based on PES scans) transition state of the S_E2' reaction between allyltrimethylsilane and oxocarbenium ions **1**-**6**. All energies (TS and TS Est.) are reported relative to the lowest energy conformer.[61,99]

species	**1**	**2**	**3**	**4**	**5-*gg***	**5-*gt***	**5-*tg***	**6**
$^3H_4$-TS-top-C	11.3	[c]	11.3	12.8	15.6	14.7	16.6	12.1
	(–1.3)	[c]	(–1.1)	(–0.1)	(2.3)	(1.8)	(3.5)	(–2.3)
$^3H_4$-TS-top-C Est.[b]	12.3	8.3	11.5	12.9	15.6	15.0	16.7	12.0
	(–0.2)	(–3.9)	(–1.2)	(–0.3)	(2.3)	(1.8)	(3.4)	(–2.3)
$^4H_3$-TS-bottom-C	[a]	7.3	11.7	11.5	11.8	11.2	12.7	11.3)
	[a]	(–4.7)	(–0.9)	(–1.5)	(–1.0)	(–1.7)	(–0.2)	(–3.0)
$^4H_3$-TS-bottom-C	[a]	7.8	11.8	11.6	11.7	11.4	12.9	11.3
Est.[b]	[a]	(–4.5)	(–0.9)	(–1.5)	(–1.4)	(–1.6)	(–0.3)	(–3.1)

[a] For the unsubstituted oxocarbenium ion **1**, the computed values are only depicted for the $^3H_4$, since both the $^3H_4$ and $^4H_3$ are chemically equivalent. [b] Estimated energies of TSs were obtained by performing frequency analysis of all non-stationary points of a relaxed PES scan, starting from the PC of which the C1•••Nuc bond was elongated in 100 steps of 0.025Å. [c] Nonexistent: barrierless process toward the product. TS = transition state, C = chair-like.

Table S6. PCM(CH_2Cl_2)-B3LYP-D3(BJ)/6-311G(d,p)//PCM(CH_2Cl_2)-B3LYP/6-311G(d,p) Gibbs energies (ΔG_{DCM}, in kcal mol^{-1}) and in parentheses electronic energies (ΔE_{DCM}, in kcal mol^{-1}) in CH_2Cl_2 relative to reactants of the transition state stationary points and the estimated (based on PES scans) transition state of the S_E2' reaction between allyltrimethylsilane and oxocarbenium ions **1**-**6**. All energies (TS and TS Est.) are reported relative to the lowest energy conformer.[61,99]

species	**1**	**2**	**3**	**4**	**5-*gg***	**5-*gt***	**5-*tg***	**6**
$^3H_4$-TS-top-C	4.8 (−7.7)	[c] [c]	3.6 (−8.8)	6.5 (−6.4)	6.3 (−6.9)	7.5 (−5.5)	9.7 (−3.3)	9.2 (−5.2)
$^3H_4$-TS-top-C Est.[b]	5.9 (−6.7)	1.2 (−10.5)	3.7 (−9.0)	6.4 (−6.9)	6.4 (−6.9)	7.6 (−5.6)	9.9 (−3.4)	9.2 (−5.2)
$^4H_3$-TS-bottom-C	[a] [a]	1.3 (−10.2)	6.1 (−6.5)	5.1 (−7.9)	5.7 (−7.2)	4.8 (−8.0)	6.5 (−6.4)	9.9 (−4.4)
$^4H_3$-TS-bottom-C Est.[b]	[a] [a]	1.0 (−10.8)	6.1 (−6.6)	5.1 (−8.0)	5.7 (−7.4)	4.8 (−8.2)	6.6 (−6.5)	10.0 (−4.5)

[a] For the unsubstituted oxocarbenium ion **1**, the computed values are only depicted for the $^3H_4$, since both the $^3H_4$ and $^4H_3$ are chemically equivalent. [b] Estimated energies of TSs were obtained by performing frequency analysis of all non-stationary points of a relaxed PES scan, starting from the PC of which the C1•••Nuc bond was elongated in 100 steps of 0.025Å. [c] Nonexistent: barrierless process toward the product. TS = transition state, C = chair-like.

Table S7. Activation strain model and energy decomposition analysis (in kcal mol^{-1}) at TS-like geometries for the for top- and bottom-attack of the S_E2' reaction between allyltrimethylsilane and cation **1**.[a]

	r C–O	ΔE^*	ΔE_{strain}	ΔE_{int}	ΔV_{elstat}	ΔE_{Pauli}	ΔE_{oi}
top-attack	1.293	–9.7	11.0	–20.7	–26.3	44.8	–38.9
bottom-attack	1.288	–5.6	11.0	–16.6	–24.5	44.1	–36.2

[a] Numerical experiment at double consistent TS-like geometries (ΔE^*) obtained from the IRC at a Si•••C bond stretch of 0.034 Å. The $C_{allyltrimethylsilane}$•••$C_{substrate}$ bond of **1** bottom-attack was set to 2.32 Å ($C_{allyltrimethylsilane}$•••$C_{substrate}$ bond in the consistent TS-like geometry for **1** top-attack). Computed at ZORA-B3LYP/TZ2P//PCM(CH_2Cl_2)-B3LYP/6-311G(d,p).

References

(1) Merino, P.; Delso, I.; Pereira, S.; Orta, S.; Pedrón, M.; Tejero, T. Computational Evidence of Glycosyl Cations. *Org. Biomol. Chem.* **2021**, *19* (11), 2350–2365.

(2) Bohé, L.; Crich, D. A Propos of Glycosyl Cations and the Mechanism of Chemical Glycosylation; the Current State of the Art. *Carbohydr. Res.* **2015**, *403*, 48–59.

(3) Walvoort, M. T. C.; Dinkelaar, J.; van den Bos, L. J.; Lodder, G.; Overkleeft, H. S.; Codée, J. D. C.; van der Marel, G. A. The Impact of Oxacarbenium Ion Conformers on the Stereochemical Outcome of Glycosylations. *Carbohydr. Res.* **2010**, *345* (10), 1252–1263.

(4) Crich, D. Mechanism of a Chemical Glycosylation Reaction. *Acc. Chem. Res.* **2010**, *43* (8), 1144–1153.

(5) Adero, P. O.; Amarasekara, H.; Wen, P.; Bohé, L.; Crich, D. The Experimental Evidence in Support of Glycosylation Mechanisms at the S_N1–S_N2 Interface. *Chem. Rev.* **2018**, *118* (17), 8242–8284.

(6) Mydock, L. K.; Demchenko, A. V. Mechanism of Chemical *O*-Glycosylation: From Early Studies to Recent Discoveries. *Org. Biomol. Chem.* **2010**, *8* (3), 497–510.

(7) Yang, M. T.; Woerpel, K. A. The Effect of Electrostatic Interactions on Conformational Equilibria of Multiply Substituted Tetrahydropyran Oxocarbenium Ions. *J. Org. Chem.* **2009**, *74* (2), 545–553.

(8) Ardèvol, A.; Rovira, C. The Molecular Mechanism of Enzymatic Glycosyl Transfer with Retention of Configuration: Evidence for a Short-Lived Oxocarbenium-Like Species. *Angew. Chem. Int. Ed.* **2011**, *50* (46), 10897–10901.

(9) Morais, M. A. B.; Coines, J.; Domingues, M. N.; Pirolla, R. A. S.; Tonoli, C. C. C.; Santos, C. R.; Correa, J. B. L.; Gozzo, F. C.; Rovira, C.; Murakami, M. T. Two Distinct Catalytic Pathways for GH43 Xylanolytic Enzymes Unveiled by X-Ray and QM/MM Simulations. *Nat. Commun.* **2021**, *12* (1), 367.

(10) Chang, C.-W.; Lin, M.-H.; Wang, C.-C. Statistical Analysis of Glycosylation Reactions. *Chem. – Eur. J.* **2021**, *27* (8), 2556–2568.

(11) Demchenko, A. V. *Handbook of Chemical Glycosylation: Advances in Stereoselectivity and Therapeutic Relevance*; Wiley-VCH: Weinheim, 2008.

(12) S. Nigudkar, S.; V. Demchenko, A. Stereocontrolled 1,2-*Cis* Glycosylation as the Driving Force of Progress in Synthetic Carbohydrate Chemistry. *Chem. Sci.* **2015**, *6* (5), 2687–2704.

(13) Hsu, C.-H.; Hung, S.-C.; Wu, C.-Y.; Wong, C.-H. Toward Automated Oligosaccharide Synthesis. *Angew. Chem. Int. Ed.* **2011**, *50* (50), 11872–11923.

(14) Chang, C.-W.; Lin, M.-H.; Wu, C.-H.; Chiang, T.-Y.; Wang, C.-C. Mapping Mechanisms in Glycosylation Reactions with Donor Reactivity: Avoiding Generation of Side Products. *J. Org. Chem.* **2020**, *85* (24), 15945–15963.

(15) Lee, J.-C.; Greenberg, W. A.; Wong, C.-H. Programmable Reactivity-Based One-Pot Oligosaccharide Synthesis. *Nat. Protoc.* **2006**, *1* (6), 3143–3152.

(16) Chen, J.; Hansen, T.; Zhang, Q.-J.; Liu, D.-Y.; Sun, Y.; Yan, H.; Codée, J. D. C.; Schmidt, R. R.; Sun, J.-S. 1-Picolinyl-5-Azido Thiosialosides: Versatile Donors for the Stereoselective Construction of Sialyl Linkages. *Angew. Chem. Int. Ed.* **2019**, *58* (47), 17000–17008.

(17) Vorm, S. van der; Hansen, T.; Hengst, J. M. A. van; Overkleeft, H. S.; Marel, G. A. van der; Codée, J. D. C. Acceptor Reactivity in Glycosylation Reactions. *Chem. Soc. Rev.* **2019**, *48* (17), 4688–4706.

(18) Demkiw, K. M.; Remmerswaal, W. A.; Hansen, T.; van der Marel, G. A.; Codée, J. D. C.; Woerpel, K. A. Halogen Atom Participation in Guiding the Stereochemical Outcomes of Acetal Substitution Reactions. *Angew. Chem. Int. Ed.* **2022**, *61*, e202209401.

(19) Hansen, T.; Lebedel, L.; Remmerswaal, W. A.; van der Vorm, S.; Wander, D. P. A.; Somers, M.; Overkleeft, H. S.; Filippov, D. V.; Désiré, J.; Mingot, A.; Bleriot, Y.; van der Marel, G. A.; Thibaudeau, S.; Codée, J. D. C. Defining the S_N1 Side of Glycosylation Reactions: Stereoselectivity of Glycopyranosyl Cations. *ACS Cent. Sci.* **2019**, *5* (5), 781–788.

(20) van der Vorm, S.; Hansen, T.; van Rijssel, E. R.; Dekkers, R.; Madern, J. M.; Overkleeft, H. S.; Filippov, D. V.; van der Marel, G. A.; Codée, J. D. C. Furanosyl Oxocarbenium Ion Conformational Energy Landscape Maps as a Tool to Study the Glycosylation Stereoselectivity of 2-Azidofuranoses, 2-Fluorofuranoses and Methyl Furanosyl Uronates. *Chem. – Eur. J.* **2019**, *25* (29), 7149–7157.

(21) Hansen, T.; Ofman, T. P.; Vlaming, J. G. C.; Gagarinov, I. A.; van Beek, J.; Goté, T. A.; Tichem, J. M.; Ruijgrok, G.; Overkleeft, H. S.; Filippov, D. V.; van der Marel, G. A.; Codée, J. D. C. Reactivity–Stereoselectivity Mapping for the Assembly of Mycobacterium Marinum Lipooligosaccharides. *Angew. Chem. Int. Ed.* **2021**, *60* (2), 937–945.

(22) van Rijssel, E. R.; van Delft, P.; Lodder, G.; Overkleeft, H. S.; van der Marel, G. A.; Filippov, D. V.; Codée, J. D. C. Furanosyl Oxocarbenium Ion Stability and Stereoselectivity. *Angew. Chem. Int. Ed.* **2014**, *53* (39), 10381–10385.

(23) Martin, A.; Arda, A.; Désiré, J.; Martin-Mingot, A.; Probst, N.; Sinaÿ, P.; Jiménez-Barbero, J.; Thibaudeau, S.; Blériot, Y. Catching Elusive Glycosyl Cations in a Condensed Phase with HF/SbF_5 Superacid. *Nat. Chem.* **2016**, *8* (2), 186–191.

(24) Elferink, H.; Severijnen, M. E.; Martens, J.; Mensink, R. A.; Berden, G.; Oomens, J.; Rutjes, F. P. J. T.; Rijs, A. M.; Boltje, T. J. Direct Experimental Characterization of Glycosyl Cations by Infrared Ion Spectroscopy. *J. Am. Chem. Soc.* **2018**, *140* (19), 6034–6038.

(25) Hansen, T.; Elferink, H.; van Hengst, J. M. A.; Houthuijs, K. J.; Remmerswaal, W. A.; Kromm, A.; Berden, G.; van der Vorm, S.; Rijs, A. M.; Overkleeft, H. S.; Filippov, D. V.; Rutjes, F. P. J. T.; van der Marel, G. A.; Martens, J.; Oomens, J.; Codée, J. D. C.; Boltje, T. J. Characterization of Glycosyl Dioxolenium Ions and Their Role in Glycosylation Reactions. *Nat. Commun.* **2020**, *11* (1), 2664.

(26) Saito, K.; Ueoka, K.; Matsumoto, K.; Suga, S.; Nokami, T.; Yoshida, J. Indirect Cation-Flow Method: Flash Generation of Alkoxycarbenium Ions and Studies on the Stability of Glycosyl Cations. *Angew. Chem. Int. Ed.* **2011**, *50* (22), 5153–5156.

(27) Lebedel, L.; Ardá, A.; Martin, A.; Désiré, J.; Mingot, A.; Aufiero, M.; Aiguabella Font, N.; Gilmour, R.; Jiménez-Barbero, J.; Blériot, Y.; Thibaudeau, S. Structural and Computational Analysis of 2-Halogeno-Glycosyl Cations in the Presence of a Superacid: An Expansive Platform. *Angew. Chem. Int. Ed.* **2019**, *58* (39), 13758–13762.

(28) Elferink, H.; Mensink, R. A.; Castelijns, W. W. A.; Jansen, O.; Bruekers, J. P. J.; Martens, J.; Oomens, J.; Rijs, A. M.; Boltje, T. J. The Glycosylation Mechanisms of 6,3-Uronic Acid Lactones. *Angew. Chem. Int. Ed.* **2019**, *58* (26), 8746–8751.

(29) Marianski, M.; Mucha, E.; Greis, K.; Moon, S.; Pardo, A.; Kirschbaum, C.; Thomas, D. A.; Meijer, G.; von Helden, G.; Gilmore, K.; Seeberger, P. H.; Pagel, K. Remote Participation during Glycosylation Reactions of Galactose Building Blocks: Direct Evidence from Cryogenic Vibrational Spectroscopy. *Angew. Chem. Int. Ed.* **2020**, *59* (15), 6166–6171.

(30) Mucha, E.; Marianski, M.; Xu, F.-F.; Thomas, D. A.; Meijer, G.; von Helden, G.; Seeberger, P. H.; Pagel, K. Unravelling the Structure of Glycosyl Cations via Cold-Ion Infrared Spectroscopy. *Nat. Commun.* **2018**, *9* (1), 4174.

(31) Remmerswaal, W. A.; Houthuijs, K. J.; van de Ven, R.; Elferink, H.; Hansen, T.; Berden, G.; Overkleeft, H. S.; van der Marel, G. A.; Rutjes, F. P. J. T.; Filippov, D. V.; Boltje, T. J.; Martens, J.; Oomens, J.; Codée, J. D. C. Stabilization of Glucosyl Dioxolenium Ions by "Dual Participation" of the 2,2-Dimethyl-2-(*Ortho*-Nitrophenyl)Acetyl (DMNPA) Protection Group for 1,2-*Cis*-Glucosylation. *J. Org. Chem.* **2022**, *87* (14), 9139–9147.

(32) Elferink, H.; Remmerswaal, W. A.; Houthuijs, K. J.; Jansen, O.; Hansen, T.; Rijs, A. M.; Berden, G.; Martens, J.; Oomens, J.; Codée, J. D. C.; Boltje, T. J. Competing C-4 and C-5-Acyl Stabilization of Uronic Acid Glycosyl Cations. *Chem. – Eur. J.* **2022**, *28*, e202201724.

(33) Hosoya, T.; Takano, T.; Kosma, P.; Rosenau, T. Theoretical Foundation for the Presence of Oxacarbenium Ions in Chemical Glycoside Synthesis. *J. Org. Chem.* **2014**, *79* (17), 7889–7894.

(34) Hosoya, T.; Kosma, P.; Rosenau, T. Theoretical Study on the Effects of a 4,6-O-Diacetal Protecting Group on the Stability of Ion Pairs from D-Mannopyranosyl and D-Glucopyranosyl Triflates. *Carbohydr. Res.* **2015**, *411*, 64–69.

(35) Huang, M.; Garrett, G. E.; Birlirakis, N.; Bohé, L.; Pratt, D. A.; Crich, D. Dissecting the Mechanisms of a Class of Chemical Glycosylation Using Primary ^{13}C Kinetic Isotope Effects. *Nat. Chem.* **2012**, *4* (8), 663–667.

(36) Nukada, T.; Bérces, A.; Wang, L.; Zgierski, M. Z.; Whitfield, D. M. The Two-Conformer Hypothesis: 2,3,4,6-Tetra-*O*-Methyl-Mannopyranosyl and -Glucopyranosyl Oxacarbenium Ions. *Carbohydr. Res.* **2005**, *340* (5), 841–852.

(37) Hansen, T.; Vermeeren, P.; Bickelhaupt, F. M.; Hamlin, T. A. Stability of Alkyl Carbocations. *Chem. Commun.* **2022**, *58* (86), 12050–12053.

(38) Ayala, L.; Lucero, C. G.; Romero, J. A. C.; Tabacco, S. A.; Woerpel, K. A. Stereochemistry of Nucleophilic Substitution Reactions Depending upon Substituent: Evidence for Electrostatic Stabilization of Pseudoaxial Conformers of Oxocarbenium Ions by Heteroatom Substituents. *J. Am. Chem. Soc.* **2003**, *125* (50), 15521–15528.

(39) Lucero, C. G.; Woerpel, K. A. Stereoselective C-Glycosylation Reactions of Pyranoses: The Conformational Preference and Reactions of the Mannosyl Cation. *J. Org. Chem.* **2006**, *71* (7), 2641–2647.

(40) Deslongchamps, P.; Dory, Y. L.; Li, S. 1994 R.U. Lemieux Award Lecture Hydrolysis of Acetals and Ketals. Position of Transition States along the Reaction Coordinates, and Stereoelectronic Effects. *Can. J. Chem.* **1994**, *72* (10), 2021–2027.

(41) Stevens, R. V.; Lee, A. W. M. Stereochemistry of the Robinson-Schoepf Reaction. A Stereospecific Total Synthesis of the Ladybug Defense Alkaloids Precoccinelline and Coccinelline. *J. Am. Chem. Soc.* **1979**, *101* (23), 7032–7035.

(42) Deslongchamps, P. *Stereoelectronic Effects in Organic Chemistry*; Pergamon: New York, 1983.

(43) Chamberland, S.; Ziller, J. W.; Woerpel, K. A. Structural Evidence That Alkoxy Substituents Adopt Electronically Preferred Pseudoaxial Orientations in Six-Membered Ring Dioxocarbenium Ions. *J. Am. Chem. Soc.* **2005**, *127* (15), 5322–5323.

(44) Romero, J. A. C.; Tabacco, S. A.; Woerpel, K. A. Stereochemical Reversal of Nucleophilic Substitution Reactions Depending upon Substituent: Reactions of Heteroatom-Substituted Six-Membered-Ring Oxocarbenium Ions through Pseudoaxial Conformers. *J. Am. Chem. Soc.* **2000**, *122* (1), 168–169.
(45) Vorm, S. van der; Hansen, T.; S. Overkleeft, H.; Marel, G. A. van der; C. Codée, J. D. The Influence of Acceptor Nucleophilicity on the Glycosylation Reaction Mechanism. *Chem. Sci.* **2017**, *8* (3), 1867–1875.
(46) Parent, J.-F.; Deslongchamps, G.; Deslongchamps, P. Bent Bond/Antiperiplanar Hypothesis: Modulating the Reactivity and the Selectivity in the Glycosylation of Bicyclic Pyranoside Models. *J. Org. Chem.* **2020**, *85* (6), 4220–4236.
(47) Me_3Si^+ eventually reacts with a TfO^- to form Me_3SiOTf in the final product (P in Table S1, S2 and S3). All stationary points, except the product, includes the energy of a single TfO^- molecule.
(48) In recent years, domain based local pair natural orbitals (DLPNO) have been used to significantly lower the computational cost, while maintaining chemical accuracy, of coupled cluster theory with single-, double-, and perturbative triple excitations (CCSD(T)).
(49) Buckle, M. J. C.; Fleming, I.; Gil, S.; Pang, K. L. C. Accurate Determinations of the Extent to Which the S_E2' Reactions of Allyl-, Allenyl- and Propargylsilanes Are Stereospecifically *Anti*. *Org. Biomol. Chem.* **2004**, *2* (5), 749–769.
(50) Buckle, M. J. C.; Fleming, I.; Gil, S. Accurate Determination of the Extent to Which an S_E2' Reaction of an Allylsilane Is *Anti*. *Tetrahedron Lett.* **1992**, *33* (31), 4479–4482.
(51) Fleming, I.; Pang, K. L. C. Determination of the Extent to Which an S_E2' Reaction of a Propargylsilane Is *Anti*. *Tetrahedron Lett.* **2002**, *43* (34), 5985–5988.
(52) Casali, E.; Porta, A.; Toma, L.; Zanoni, G. Oxo-Rhenium-Mediated Allylation of Furanoside Derivatives: A Computational Study on the Mechanism and the Stereoselectivity. *J. Org. Chem.* **2022**, *87* (15), 9497–9506.
(53) Vermeeren, P.; van der Lubbe, S. C. C.; Fonseca Guerra, C.; Bickelhaupt, F. M.; Hamlin, T. A. Understanding Chemical Reactivity Using the Activation Strain Model. *Nat. Protoc.* **2020**, *15* (2), 649–667.
(54) Bickelhaupt, F. M.; Houk, K. N. Analyzing Reaction Rates with the Distortion/Interaction-Activation Strain Model. *Angew. Chem. Int. Ed.* **2017**, *56* (34), 10070–10086.
(55) Bickelhaupt, F. M.; Baerends, E. J. Kohn-Sham Density Functional Theory: Predicting and Understanding Chemistry. In *Reviews in Computational Chemistry*; John Wiley & Sons, Ltd: New York, 2000; pp 1–86.
(56) van Meer, R.; Gritsenko, O. V.; Baerends, E. J. Physical Meaning of Virtual Kohn–Sham Orbitals and Orbital Energies: An Ideal Basis for the Description of Molecular Excitations. *J. Chem. Theory Comput.* **2014**, *10* (10), 4432–4441.
(57) Hamlin, T. A.; Vermeeren, P.; Guerra, C. F.; Bickelhaupt, F. M. Energy Decomposition Analysis in the Context of Quantitative Molecular Orbital Theory. In *Complementary Bonding Analysis*; De Gruyter, 2021; pp 199–212.
(58) The dispersion-corrected PCM(CH_2Cl_2)-B3LYP-D3(BJ)/6-311G(d,p) approach rendered proivides reactivity trends compared to PCM(CH_2Cl_2)-B3LYP/6-311G(d,p) (Table S3 and S6).
(59) Seeman, J. I. The Curtin-Hammett Principle and the Winstein-Holness Equation: New Definition and Recent Extensions to Classical Concepts. *J. Chem. Educ.* **1986**, *63* (1), 42.
(60) Seeman, J. I. Effect of Conformational Change on Reactivity in Organic Chemistry. Evaluations, Applications, and Extensions of Curtin-Hammett Winstein-Holness Kinetics. *Chem. Rev.* **1983**, *83* (2), 83–134.
(61) Peng, Q.; Duarte, F.; Paton, R. S. Computing Organic Stereoselectivity – from Concepts to Quantitative Calculations and Predictions. *Chem. Soc. Rev.* **2016**, *45* (22), 6093–6107.
(62) Vermeeren, P.; Hansen, T.; Jansen, P.; Swart, M.; Hamlin, T. A.; Bickelhaupt, F. M. A Unified Framework for Understanding Nucleophilicity and Protophilicity in the S_N2/E2 Competition. *Chem. – Eur. J.* **2020**, *26* (67), 15538–15548.
(63) Vermeeren, P.; Hansen, T.; Grasser, M.; Silva, D. R.; Hamlin, T. A.; Bickelhaupt, F. M. S_N2 versus E2 Competition of F^- and PH_2^- Revisited. *J. Org. Chem.* **2020**, *85* (21), 14087–14093.
(64) Hansen, T.; Roozee, J. C.; Bickelhaupt, F. M.; Hamlin, T. A. How Solvation Influences the S_N2 versus E2 Competition. *J. Org. Chem.* **2022**, *87* (3), 1805–1813.
(65) Hansen, T.; Vermeeren, P.; Bickelhaupt, F. M.; Hamlin, T. A. Origin of the α-Effect in S_N2 Reactions. *Angew. Chem. Int. Ed.* **2021**, *60* (38), 20840–20848.
(66) Hansen, T.; Vermeeren, P.; de Jong, L.; Bickelhaupt, F. M.; Hamlin, T. A. S_N2 versus S_N2' Competition. *J. Org. Chem.* **2022**, *87* (14), 8892–8901.
(67) Hansen, T.; Nin-Hill, A.; Codée, J. D. C.; Hamlin, T. A.; Rovira, C. Rational Tuning of the Reactivity of Three-Membered Heterocycle Ring Openings via S_N2 Reactions. *Chem. – Eur. J.* **2022**, *28* (60), e202201649.
(68) Hansen, T.; Sun, X.; Dalla Tiezza, M.; van Zeist, W.-J.; van Stralen, J. N. P.; Geerke, D. P.; Wolters, L. P.; Poater, J.; Hamlin, T. A.; Bickelhaupt, F. M. C–X Bond Activation by Palladium: Steric Shielding versus Steric Attraction. *Chem. – Eur. J.* **2022**, *28* (44), e202201093.
(69) Installing an OMe-substituent at the C5-position, instead of the C5-CH_2OMe-substituent, results in more similar behavior as found for cation **3** and **4** (see SI Figure S1, S2 and SI Table S1 and S2 for data), in

which the difference in strain of the oxocarbenium ions at the start of the reaction profile can be directly attributed to the conformational preference of the cation.

(70) Frisch, M. J.; Trucks, G. W.; Cheeseman, J. R.; Scalmani, G.; Caricato, M.; Hratchian, H. P.; Li, X.; Barone, V.; Bloino, J.; Zheng, G.; Vreven, T.; Montgomery, J. A.; Petersson, G. A.; Scuseria, G. E.; Schlegel, H. B.; Nakatsuji, H.; Izmaylov, A. F.; Martin, R. L.; Sonnenberg, J. L.; Peralta, J. E.; Heyd, J. J.; Brothers, E.; Ogliaro, F.; Bearpark, M.; Robb, M. A.; Mennucci, B.; Kudin, K. N.; Staroverov, V. N.; Kobayashi, R.; Normand, J.; Rendell, A.; Gomperts, R.; Zakrzewski, V. G.; Hada, M.; Ehara, M.; Toyota, K.; Fukuda, R.; Hasegawa, J.; Ishida, M.; Nakajima, T.; Honda, Y.; Kitao, O.; Nakai, H. Gaussian 09 Rev. D.01, 2009.

(71) Becke, A. D. Density-functional Thermochemistry. III. The Role of Exact Exchange. *J. Chem. Phys.* **1993**, *98* (7), 5648–5652.

(72) Lee, C.; Yang, W.; Parr, R. G. Development of the Colle-Salvetti Correlation-Energy Formula into a Functional of the Electron Density. *Phys. Rev. B Condens. Matter* **1988**, *37* (2), 785–789.

(73) Vosko, S. H.; Wilk, L.; Nusair, M. Accurate Spin-Dependent Electron Liquid Correlation Energies for Local Spin Density Calculations: A Critical Analysis. *Can. J. Phys.* **1980**, *58* (8), 1200–1211.

(74) Ditchfield, R.; Hehre, W. J.; Pople, J. A. Self-Consistent Molecular-Orbital Methods. IX. An Extended Gaussian-Type Basis for Molecular-Orbital Studies of Organic Molecules. *J. Chem. Phys.* **1971**, *54* (2), 724–728.

(75) Bootsma, A. N.; Wheeler, S. Popular Integration Grids Can Result in Large Errors in DFT-Computed Free Energies. ChemRxiv July 29, 2019.

(76) Riplinger, C.; Sandhoefer, B.; Hansen, A.; Neese, F. Natural Triple Excitations in Local Coupled Cluster Calculations with Pair Natural Orbitals. *J. Chem. Phys.* **2013**, *139* (13), 134101.

(77) Liakos, D. G.; Sparta, M.; Kesharwani, M. K.; Martin, J. M. L.; Neese, F. Exploring the Accuracy Limits of Local Pair Natural Orbital Coupled-Cluster Theory. *J. Chem. Theory Comput.* **2015**, *11* (4), 1525–1539.

(78) Guo, Y.; Riplinger, C.; Becker, U.; Liakos, D. G.; Minenkov, Y.; Cavallo, L.; Neese, F. Communication: An Improved Linear Scaling Perturbative Triples Correction for the Domain Based Local Pair-Natural Orbital Based Singles and Doubles Coupled Cluster Method [DLPNO-CCSD(T)]. *J. Chem. Phys.* **2018**, *148* (1), 011101.

(79) Neese, F. The ORCA Program System. *WIREs Comput. Mol. Sci.* **2012**, *2* (1), 73–78.

(80) Neese, F. Software Update: The ORCA Program System—Version 5.0. *WIREs Comput. Mol. Sci.* **2022**, *12* (5), e1606.

(81) Sun, X.; Soini, T. M.; Poater, J.; Hamlin, T. A.; Bickelhaupt, F. M. PyFrag 2019—Automating the Exploration and Analysis of Reaction Mechanisms. *J. Comput. Chem.* **2019**, *40* (25), 2227–2233.

(82) Legault, C. Y. CYLview, 1.0b, Université de Sherbrooke, 2009. http://www.cylview.org.

(83) Ribeiro, R. F.; Marenich, A. V.; Cramer, C. J.; Truhlar, D. G. Use of Solution-Phase Vibrational Frequencies in Continuum Models for the Free Energy of Solvation. *J. Phys. Chem. B* **2011**, *115* (49), 14556–14562.

(84) Luchini, G.; Alegre-Requena, J. V.; Funes-Ardoiz, I.; Paton, R. S. GoodVibes: Automated Thermochemistry for Heterogeneous Computational Chemistry Data. *F1000Research* **2020**, *9*, 291.

(85) Fonseca Guerra, C.; Snijders, J. G.; te Velde, G.; Baerends, E. J. Towards an Order-N DFT Method. *Theor. Chem. Acc.* **1998**, *99* (6), 391–403.

(86) te Velde, G.; Bickelhaupt, F. M.; Baerends, E. J.; Fonseca Guerra, C.; van Gisbergen, S. J. A.; Snijders, J. G.; Ziegler, T. Chemistry with ADF. *J. Comput. Chem.* **2001**, *22* (9), 931–967.

(87) Baerends, E. J.; Ziegler, T.; Atkins, A. J.; Autschbach, J.; Bashford, D.; Baseggio, O.; Bérces, A.; Bickelhaupt, F. M.; Bo, C.; Boerritger, P. M.; Cavallo, L.; Daul, C.; Chong, D. P.; Chulhai, D. V.; Deng, L.; Dickson, R. M.; Dieterich, J. M.; Ellis, D. E.; van Faassen, M.; Ghysels, A.; Giammona, A.; van Gisbergen, S. J. A.; Goez, A.; Götz, A. W.; Gusarov, S.; Harris, F. E.; van den Hoek, P.; Hu, Z.; Jacob, C. R.; Jacobsen, H.; Jensen, L.; Joubert, L.; Kaminski, J. W.; van Kessel, G.; König, C.; Kootstra, F.; Kovalenko, A.; Krykunov, M.; van Lenthe, E.; McCormack, D. A.; Michalak, A.; Mitoraj, M.; Morton, S. M.; Neugebauer, J.; Nicu, V. P.; Noodleman, L.; Osinga, V. P.; Patchkovskii, S.; Pavanello, M.; Peeples, C. A.; Philipsen, P. H. T.; Post, D.; Pye, C. C.; Ramanantoanina, H.; Ramos, P.; Ravenek, W.; Rodríguez, J. I.; Ros, P.; Rüger, R.; Schipper, P. R. T.; Schlüns, D.; van Schoot, H.; Schreckenbach, G.; Seldenthuis, J. S.; Seth, M.; Snijders, J. G.; Solà, M.; M, S.; Swart, M.; Swerhone, D.; te Velde, G.; Tognetti, V.; Vernooijs, P.; Versluis, L.; Visscher, L.; Visser, O.; Wang, F.; Wesolowski, T. A.; van Wezenbeek, E. M.; Wiesenekker, G.; Wolff, S. K.; Woo, T. K.; Yakovlev, A. L. ADF2017, SCM, Theoretical Chemistry, Vrije Universiteit, Amsterdam, The Netherlands, https://www.scm.com.

(88) Van Lenthe, E.; Baerends, E. J. Optimized Slater-Type Basis Sets for the Elements 1–118. *J. Comput. Chem.* **2003**, *24* (9), 1142–1156.

(89) Franchini, M.; Philipsen, P. H. T.; van Lenthe, E.; Visscher, L. Accurate Coulomb Potentials for Periodic and Molecular Systems through Density Fitting. *J. Chem. Theory Comput.* **2014**, *10* (5), 1994–2004.

(90) Franchini, M.; Philipsen, P. H. T.; Visscher, L. The Becke Fuzzy Cells Integration Scheme in the Amsterdam Density Functional Program Suite. *J. Comput. Chem.* **2013**, *34* (21), 1819–1827.

(91) Lenthe, E. van; Baerends, E. J.; Snijders, J. G. Relativistic Regular Two-component Hamiltonians. *J. Chem. Phys.* **1993**, *99* (6), 4597–4610.

(92) van Lenthe, E.; Baerends, E. J.; Snijders, J. G. Relativistic Total Energy Using Regular Approximations. *J. Chem. Phys.* **1994**, *101* (11), 9783–9792.

(93) Beek, B. van; Bochove, M. A. van; Hamlin, T. A.; Bickelhaupt, F. M. Nucleophilic Substitution at Di- and Triphosphates: Leaving Group Ability of Phosphate versus Diphosphate. *Electron. Struct.* **2019**, *1* (2), 024001.

(94) Galabov, B.; Koleva, G.; Schaefer III, H. F.; Allen, W. D. Nucleophilic Influences and Origin of the S_N2 Allylic Effect. *Chem. – Eur. J.* **2018**, *24* (45), 11637–11648.

(95) Hansen, T.; Vermeeren, P.; Yoshisada, R.; Filippov, D. V.; van der Marel, G. A.; Codée, J. D. C.; Hamlin, T. A. How Lewis Acids Catalyze Ring-Openings of Cyclohexene Oxide. *J. Org. Chem.* **2021**, *86* (4), 3565–3573.

(96) Ryu, H.; Park, J.; Kim, H. K.; Park, J. Y.; Kim, S.-T.; Baik, M.-H. Pitfalls in Computational Modeling of Chemical Reactions and How To Avoid Them. *Organometallics* **2018**, *37* (19), 3228–3239.

(97) Bao, J. L.; Zhang, X.; Truhlar, D. G. Barrierless Association of CF_2 and Dissociation of C_2F_4 by Variational Transition-State Theory and System-Specific Quantum Rice–Ramsperger–Kassel Theory. *Proc. Natl. Acad. Sci.* **2016**, *113* (48), 13606–13611.

(98) de M. Oliveira, R. C.; Bauerfeldt, G. F. Implementation of a Variational Code for the Calculation of Rate Constants and Application to Barrierless Dissociation and Radical Recombination Reactions: CH_3OH = CH_3 + OH. *Int. J. Quantum Chem.* **2012**, *112* (19), 3132–3140.

(99) If $\Delta G°_{3H4} < \Delta G°_{4H3}$ then $\Delta\Delta G^{‡}_{\text{addition}} = \Delta G^{‡}_{\text{top}} - (\Delta G^{‡}_{\text{bottom}} + \Delta\Delta G°)$, while if $\Delta G°_{3H4} > \Delta G°_{4H3}$ then $\Delta\Delta G^{‡}_{\text{addition}} = (\Delta G^{‡}_{\text{top}} + \Delta\Delta G°) - \Delta G^{‡}_{\text{bottom}}$ according to the work of the Paton group.